Vacuum-Referred Binding Energies of Bismuth and Lanthanide Levels in ARE(Si,Ge)O_4 (A = Li, Na; RE = Y, Lu)

Toward Designing Charge-Carrier-Trapping Processes for Energy Storage

Lyu, Tianshuai; Dorenbos, Pieter

DOI
10.1021/acs.chemmater.9b04341

Publication date
2020

Document Version
Final published version

Published in
Chemistry of Materials

CHEMISTRY OF MATERIALS

pubs.acs.org/cm

Article

Vacuum-Referred Binding Energies of Bismuth and Lanthanide Levels in ARE(Si,Ge)O_4 (A = Li, Na; RE = Y, Lu): Toward Designing Charge-Carrier-Trapping Processes for Energy Storage

Tianshuai Lyu* and Pieter Dorenbos

Cite This: *Chem. Mater.* 2020, 32, 1192−1209

Read Online

ACCESS | Metrics & More | Article Recommendations | Supporting Information

ABSTRACT: Developing a feasible design principle for solid-state materials for persistent luminescence and storage phosphors with high charge carrier storage capacity remains a crucial challenge. Here we report a methodology for such rational design via vacuum referred binding energy (VRBE) diagram aided band structure engineering and crystal synthesis optimization. The ARE(Si,Ge)O_4 (A = Li, Na; RE = Y, Lu) crystal system was selected as a model example. Low-temperature (10 K) photoluminescence excitation and emission spectra of bismuth- and lanthanide-doped ARE(Si,Ge)O_4 system were first systematically studied, and the corresponding VRBE schemes were then established. Guided by these VRBE schemes, Bi^{3+} afterglow and storage phosphor properties were explored in $NaLu_{1-x}Y_xGeO_4$. By combining Bi^{3+} with Bi^{3+} itself or Eu^{3+}, Bi^{3+} appears to act as a deep hole-trapping center, while Bi^{3+} and Eu^{3+} act as less-deep electron traps. Trap depth tunable afterglow and storage were realized in $NaLu_{1-x}Y_xGeO_4$:0.01Bi^{3+} and $NaLu_{1-x}Y_xGeO_4$:0.01Bi^{3+},0.001Eu^{3+} by adjusting *x*, leading to conduction band engineering. More than 28 h of persistent luminescence of Bi^{3+} was measurable in $NaYGeO_4$:0.01Bi^{3+} due to electron release from Bi^{2+} and recombination with a hole at Bi^{4+}. The charge carrier storage capacity in $NaYGeO_4$:0.01Bi^{3+} was discovered to increase ∼7 times via optimizing synthesis condition at 1200 °C during 24 h. The thermoluminescence (TL) intensity of the optimized $NaYGeO_4$:0.001Bi^{3+} and $NaYGeO_4$:0.01Bi^{3+},0.001Eu^{3+} is ∼3, and ∼7 times higher than the TL of the state-of-the-art X-ray storage phosphor BaFBr(I):Eu. Proof-of-concept color tuning for anti-counterfeiting application was demonstrated by combining the discovered and optimized $NaYGeO_4$:0.01Bi^{3+} afterglow phosphor with perovskite $CsPbBr_3$ and CdSe quantum dots. Information storage application was demonstrated by UV-light- or X-ray-charged $NaYGeO_4$:0.01Bi^{3+},0.001Eu^{3+} phosphor dispersed in a silicone gel imaging film. This work not only reports excellent storage phosphors but more importantly provides a design principle that can initiate more exploration of afterglow and storage phosphors in a designed way through combining VRBE-scheme-guided band structure engineering and crystal synthesis optimization.

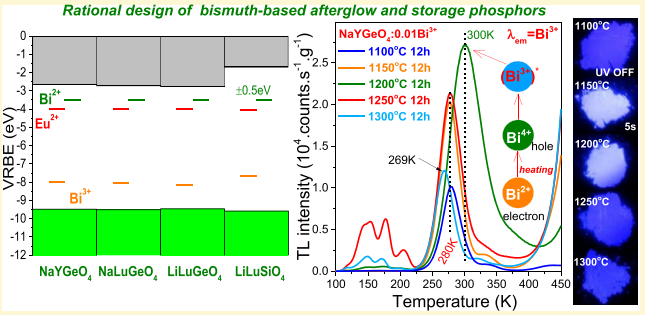

1. INTRODUCTION

Storage phosphors are information storage materials that capture electrons and holes in host defect traps after exposure to ionizing radiation.[1−5] They have widespread applications, like in dosimetry of X-rays, electrons, or γ-rays;[6−9] digital dental radiograph imaging systems;[10] and computed radiography (CR) using X-ray-charged storage phosphor film.[11,12] Like a storage phosphor, an afterglow phosphor is another type of energy storage material that can first capture charge carriers in defect trap(s) upon absorbing excitation energy, but then it can gradually emit photons when excitation radiation is removed.[13,14] Afterglow phosphors are proposed to be used in anti-counterfeiting applications because the afterglow color and/or intensity may change as a function of time in the dark.[15−18] To date, few really good afterglow and storage phosphors have been discovered. One of the important reasons is that a majority of research work is based on an approach by trial and error, and the charge-carrier-trapping processes are often not deeply and systematically studied. This does not provide enough insights and guidance for further research. Developing an effective design principle in solid-state materials for persistent luminescence and storage phosphors with high charge carrier storage capacity is a challenge.

A persistent luminescence or storage phosphor is constituted of the compound lattice, the recombination center, and the electron- and hole-capturing centers that are often lattice impurities or intrinsic defect(s).[19] The properties

Received: October 23, 2019
Revised: January 6, 2020
Published: January 6, 2020

of the recombination centers and the host lattices determine the emission decay time and the emitting wavelength, which can change from deep ultraviolet to even infrared. The trap depths of the electron- and hole-trapping centers and their distribution within the compound lattice decide how long the electrons and holes are trapped. For a persistent luminescence phosphor, shallow traps (<~0.7 eV) are required to produce thermally stimulated afterglow at room temperature (RT).[19,20] For a storage phosphor, deep traps (>~1 eV) are required to avoid energy loss via thermal fading at RT.[5,11] Rational design of afterglow and storage phosphors is possible if one can tailor the trap depths of the electron- and hole-capturing centers. If the charge carrier storage capacity can further be optimized by synthesis conditions, then a good storage phosphor may appear.

In X-ray computed radiography, the image information of patients is first stored in a storage phosphor imaging film and then read out by scanning the film point-by-point with a stimulation photon source like a solid-state laser beam with wavelength ranging from 375 to 1800 nm.[21,22] The photostimulated light is rapidly recorded with a photomultiplier tube that has a high quantum efficiency from 300 to 450 nm. In current flying-spot computed radiography digitizers, the read-out time for each pixel is less than 2 μs.[11] The light emission from the phosphor at the previous pixel should have decayed to at least 1/e of its initial emission intensity when the phosphor at the present pixel is stimulated. Therefore, for use in flying-spot scanners, the decay time of a recombination center in a storage phosphor should be <~2 μs. Other requirements for a good storage phosphor for computed radiography, as proposed in refs 11 and 22, are high X-ray absorption and conversion efficiency to trapped electrons and holes, slow fading, good chemical stability, and the optical erasure ability of stored information. Today BaFBr(I):Eu is the state-of-the-art X-ray storage phosphor.[12,23−25] Unfortunately, its durability is limited because it is hygroscopic. The exploration of better storage phosphors is going on.[26−28] Recently, Dobrowolska et al.[5] reported an excellent storage phosphor, $LiLuSiO_4$:Ce,Tm, with high charge carrier storage capacity using a typical trial-and-error approach. However, the nature of the trap(s) in $LiLuSiO_4$:Ce,Tm still remains unknown, and design principles for storage phosphors were not proposed.

For afterglow phosphors, most of the research work is focused on Eu^{2+}-, Ce^{3+}-, or Cr^{3+}-doped compounds.[29−31] Bismuth-based materials are of current research interest because of their promising applications in various fields like in semiconductors,[32] quantum dots,[33] or topological insulators.[34] Particularly, Bi^{3+} as an emission center has been widely used in photoluminescence phosphors.[35−37] However, Bi^{3+}-based afterglow or storage phosphor development is rarely reported.[38−40] Recently, Wang et al.[41] reported the persistent luminescence of Bi^{3+} in Bi^{3+}- and Eu^{3+}-doped $NaLuGeO_4$. The charge-carrier-trapping processes are not fully clear because Bi^{3+} may act as a hole trap but also as an electron trap. A deep understanding of the electron- and hole-trapping processes in bismuth-doped compounds will be helpful to accelerate the exploration of better afterglow and storage phosphors.

Methods were proposed to determine the locations of the divalent and trivalent lanthanides, Bi^{3+}, or Bi^{2+} energy levels within the band gap of inorganic compounds.[42−45] With spectroscopic data, one may construct a vacuum-referred binding energy (VRBE) scheme.[46] Knowledge on the VRBE in defect levels like lanthanides, valence band (VB), conduction band (VB), or bismuth then offers an effective way to predict, understand, and even tailor electron- and hole-capturing processes. Up to now, the VRBE-guided method has mainly been applied to explore afterglow phosphors in lanthanide and/or Cr^{3+}-doped garnet compounds,[29] and only a few good afterglow phosphors were developed. Particularly, to the best of our knowledge, there is rare reporting on the design of Bi^{3+} afterglow or storage phosphor by a combination of VRBE-aided band structure engineering and optimizing crystal synthesis conditions.

The objective of this work is to show how to design Bi^{3+} afterglow and storage phosphors using VRBE-aided band structure engineering and crystal synthesis optimization. Because of the good storage properties of $LiLuSiO_4$, the $ARE(Si,Ge)O_4$ (A = Li, Na; RE = Y, Lu) family of materials was selected for further research. Low-temperature (10 K) photoluminescence excitation and emission spectra of the bismuth- and lanthanide-doped $ARE(Si,Ge)O_4$ system were first systematically investigated, and the corresponding VRBE schemes were then established, like in Figure 1, which act as a basis for our research. Figure 1a predicts how the electron- or hole-trapping depth can be tailored by changing the conduction band or valence band energies with crystal composition modulation. Figure 1b helps to select potential combinations of hole- and electron-capturing centers. To demonstrate the design principle, in this work, we will mainly

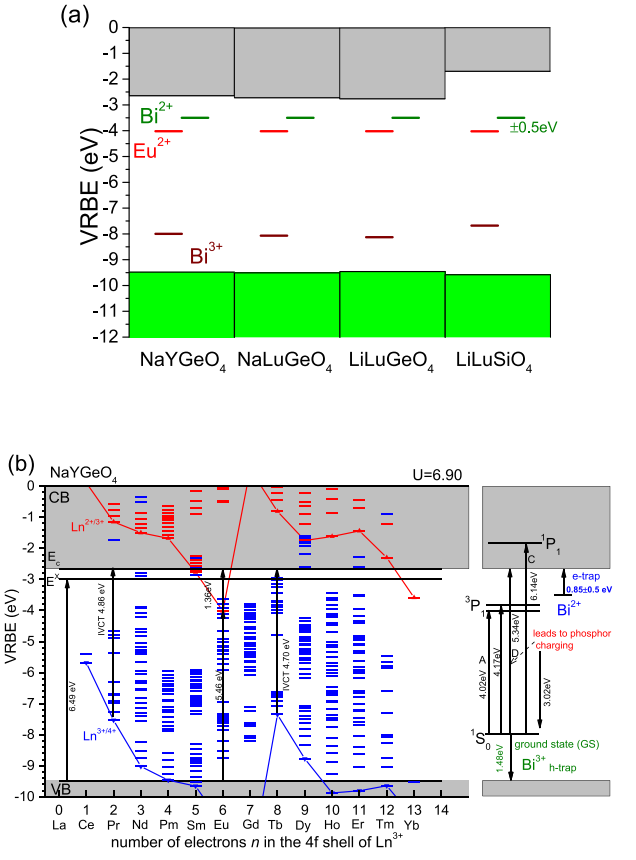

Figure 1. Vacuum-referred binding energy (VRBE) diagrams of (a) the $NaYGeO_4$-related family of compounds and (b) $NaYGeO_4$, including the VRBE in the ground states of lanthanides, Bi^{2+}, and Bi^{3+}. Arrows indicate experimentally observed transitions.

https://dx.doi.org/10.1021/acs.chemmater.9b04341
Chem. Mater. 2020, 32, 1192−1209

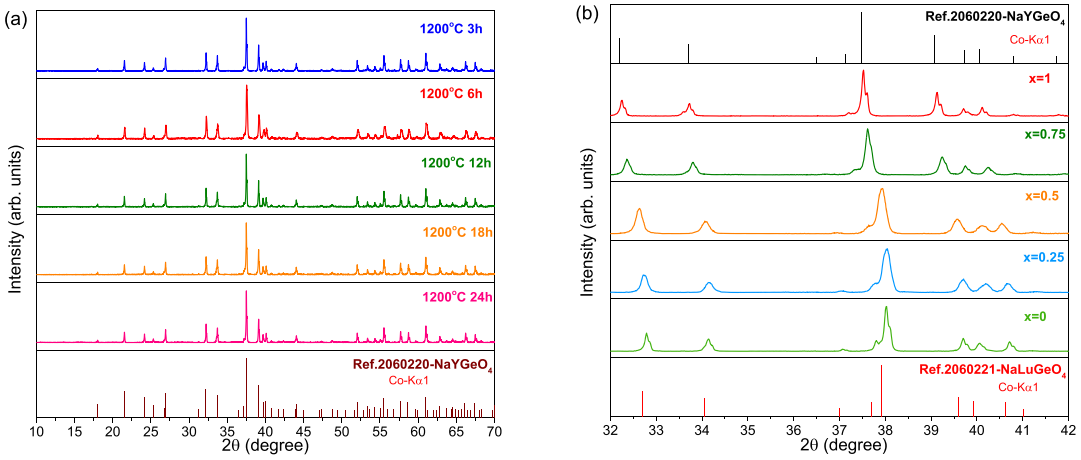

Figure 2. XRD patterns for (a) $NaYGeO_4$:0.01Bi^{3+} synthesized at 1200 °C during 3−24h and (b) $NaLu_{1-x}Y_xGeO_4$:0.01Bi^{3+},0.001Eu^{3+} (x = 0−1) solid solutions.

focus on $NaLu_{1-x}Y_xGeO_4$ crystals and study the charge-trapping processes regarding bismuth and europium in detail. The effects of crystal synthesis optimization on charge carrier storage capacity were studied in $NaYGeO_4$:0.01Bi^{3+}. Proof-of-concept color tuning for anti-counterfeiting application was demonstrated by combining the discovered $NaYGeO_4$:0.01Bi^{3+} afterglow phosphor with perovskite $CsPbBr_3$ and CdSe quantum dots. Information storage application was demonstrated by an UV-light- and X-ray-charged $NaYGeO_4$:0.01Bi^{3+},0.001Eu^{3+} phosphor dispersed in a silicone gel imaging film.

2. EXPERIMENTAL SECTION

SiO_2 (99.99%) crystals with 0.2−0.7 mm dimension were purchased from Umicore and ground into fine particles. Other starting chemicals were purchased from Sigma-Aldrich and utilized without further treatment. A series of Bi^{3+}- and/or lanthanide-activated compounds, $NaLu_{1-x}Y_xGeO_4$, $Na_{1-x}Li_xLuGeO_4$, $LiLuSi_{1-x}Ge_xO_4$, $LiLu_{0.25}Y_{0.75}Si_{1-x}Ge_xO_4$, and $LiLu_{1-x}Y_xSiO_4$, were synthesized via typical high-temperature solid-state reactions. For the compounds containing Li, an excess of 10% Li^+ above the normal stoichiometry was added to compensate for the loss of Li^+ at high temperature. The appropriate mixtures of SiO_2 (99.99%), GeO_2 (99.99%), Li_2CO_3 (99.99%), Na_2CO_3 (99.99%), and other rare earth oxides with high purity of 4 N (99.99%) were mixed well and then fired in corundum crucibles under ambient atmosphere at 800 °C for 8 h and then 1150 °C for 12 h. Finally, the obtained crystals were naturally cooled to room temperature (RT) and then ground into homogeneous powders before further measurements. The applied heating rate of the furnace is 3 °C/min. Particularly, to optimize the persistent luminescence of Bi^{3+} in $NaYGeO_4$:0.01Bi^{3+}, its synthesis conditions were explored by changing the temperature from 1100 to 1300 °C and the duration time from 3 to 24 h.

All crystals were identified using a PANalytical XPert PRO X-ray diffraction setup equipped with a Co Kα (λ = 0.178 901 nm) X-ray tube operated at 45 kV and 40 mA. The recorded X-ray diffraction (XRD) patterns were compared with the standard reference from Pearson's Crystal Database. The photoluminescence (PL) emission and excitation (PLE) spectra were measured by utilizing a system that includes a VUV/UV branch using a water-cooled deuterium (D_2) lamp with an ARC VM505 vacuum monochromator and a UV/vis branch utilizing a 500 W Hamamatsu CW Xe lamp with a Gemini 180 monochromator. A PerkinElmer MP-1913 photomultiplier was employed as the signal detector. The crystals can be cooled to 10 K by utilizing a closed helium cryostat (HC-4) with a Lake Shore 331 temperature controller in vacuum. All shown PLE spectra have been corrected by the incident photon flux. The fluorescence decay curves were recorded using the above PL setup that further combines a wavelength tunable YAG:Nd laser system (NT230-100-SH/DUV-SCU) with a digitizer module.

High-temperature thermoluminescence (TL) glow curves (300−823 K) were measured with a setup that contains an EMI 9635QA photomultiplier tube, a RISØ TL/OSL reader (model DA-15), and a DA-20 controller. All crystals were first heated to 823 K three times to empty all traps and then cooled to RT followed by β-irradiation utilizing a $^{90}Sr/^{90}Y$ source with a dose rate of ∼0.7 mGy/s under nitrogen gas in darkness. Low-temperature TL glow curves (LTTL) between 90 and 450 K were measured using a facility that contains a PerkinElmer channel photomultiplier tube (MP-1393) and a $^{90}Sr/^{90}Y$ β-irradiation source with a dose rate of ∼0.4 mGy/s. Prior to the LTTL measurements at a heating rate of 1 K/s, powder samples were pressed into pills with an area ∼0.2 cm^2 and mass <∼5 mg. The pills were attached to a metal unit with heating elements by silver paint. The pills were first heated to 450 K for 3 min in darkness and then cooled to 90 K using liquid nitrogen followed by 600 s β-irradiation in a vacuum (10^{-7} mbar). A 400 nm bandpass filter (400FS40-50, Andover Corp.) was placed between the PM tube and the pills to select the characteristic Bi^{3+} emission in $NaLu_{1-x}Y_xGeO_4$:0.01Bi^{3+}. All measured TL glow curves have been corrected by the sample mass and β-irradiation time, and glow intensity is expressed in counts/g/s, where counts are an instrumental unit.

Thermoluminescence emission (TLEM) spectra were measured with a facility that combines a UV/vis QE65000 spectrometer with a RISØ TL/OSL reader. The powder samples were heated to 823 K to empty all traps and then cooled to RT followed by γ-irradiation from a ^{60}Co source to an absorbed dose of ∼2.5 kGy. The TLEM spectra recorded by QE65000 have been corrected by its wavelength-dependent quantum efficiency.

Thermoluminescence excitation (TLE) spectra were performed by first charging the crystals during 300 s with monochromatic photons produced by a 150 W xenon arc lamp (Hamamatsu L2273) that was filtered with a monochromator (Oriel Cornerstone 130). The TLE facility has a wavelength resolution of 8 nm against a 1 mm slit width. Here, the slit width was fixed to 1 mm and the wavelength step was set as 10 nm for all TLE measurements in this work. The TLE facility was programmed by LabVIEW to measure all TL glow from RT to 723 K at a heating rate of 5 K/s at illumination wavelengths from 200 to 400 nm. A so-called TLE plot like that in Figure 9c was constructed by integrating the intensity of a TL glow peak and displaying it versus the charging wavelength.[19,47] A 400 nm bandpass filter (400FS40-50) was used to monitor Bi^{3+} emission. All recorded TLE curves have been corrected for the charging time, sample mass, and wavelength-dependent excitation intensity of the xenon arc lamp.

The photographs of Bi^{3+}-related emission were taken with an iPhone 8Plus. A Hg lamp with the main emission near 254 nm was

https://dx.doi.org/10.1021/acs.chemmater.9b04341
Chem. Mater. 2020, 32, 1192−1209

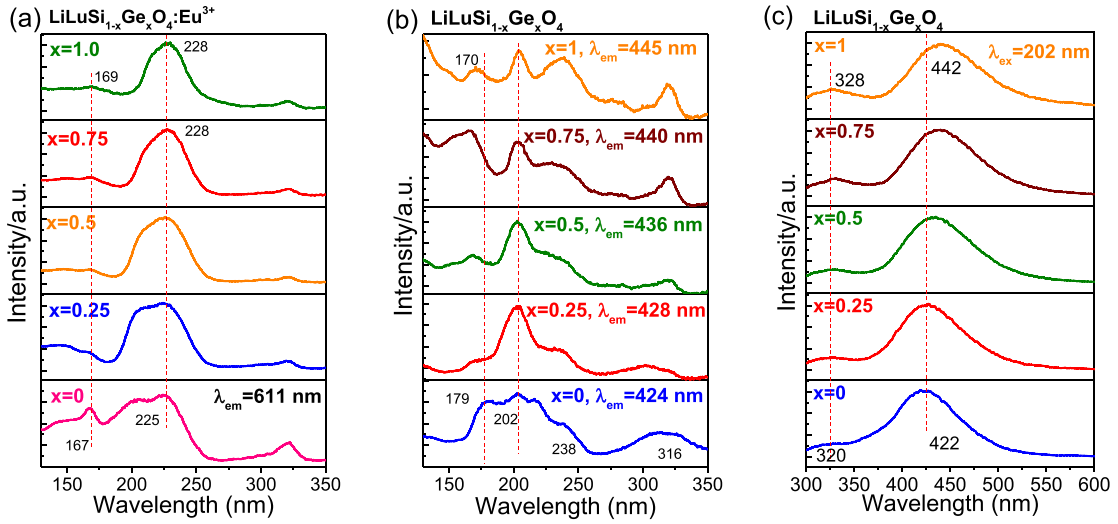

Figure 3. Photoluminescence excitation (PLE) and emission (PL) spectra for (a) $LiLuSi_{1-x}Ge_xO_4$:0.01Eu^{3+} monitoring Eu^{3+} emission at 611 nm and (b, c) undoped $LiLuSi_{1-x}Ge_xO_4$ at 10 K.

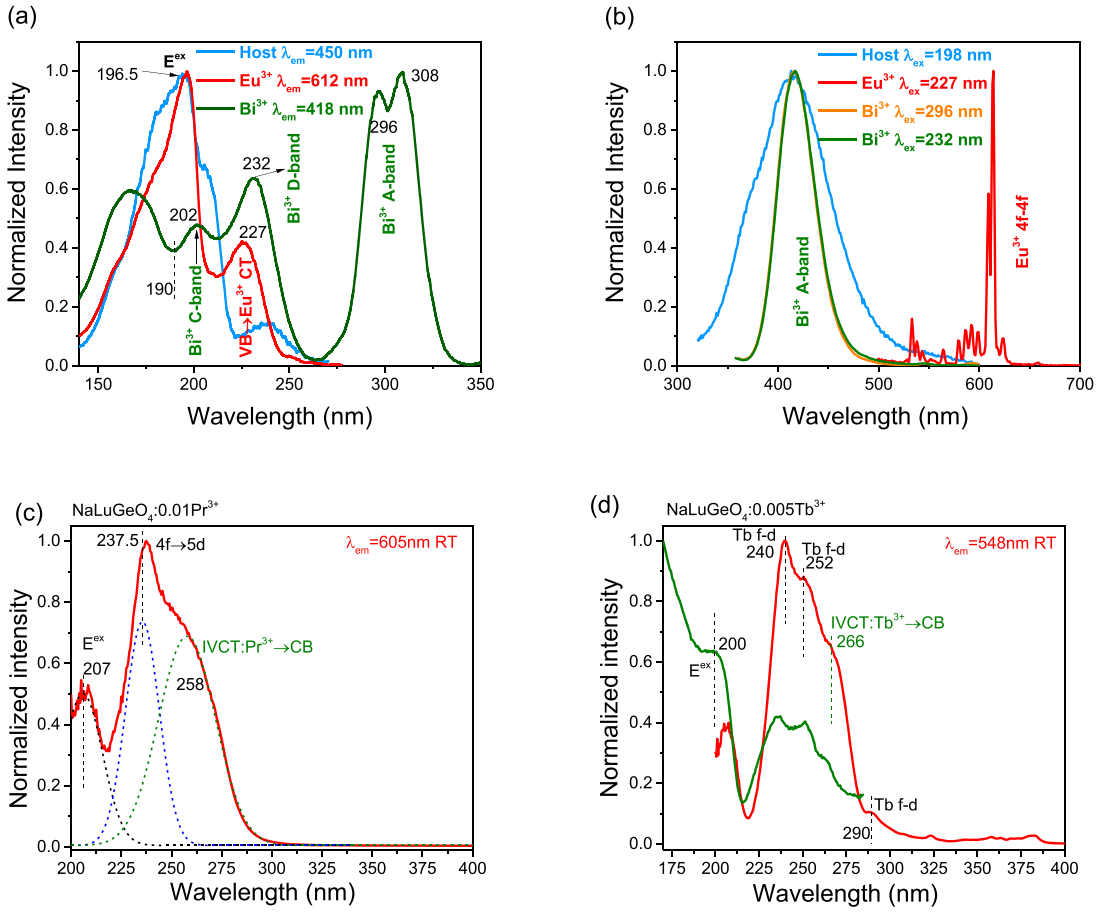

Figure 4. Photoluminescence excitation (PLE) and emission spectra for (a, b) $NaLuGeO_4$ host, $NaLuGeO_4$:0.01Bi^{3+}, and $NaLuGeO_4$:0.01Eu^{3+} at 10 K and PLE spectra for (c) $NaLuGeO_4$:0.01Pr^{3+} and (d) $NaLuGeO_4$:0.005Tb^{3+} at RT.

utilized to charge $NaYGeO_4$:0.01Bi^{3+}. For the phosphor dispersed in a silicone gel, appropriate mixtures of phosphor and silicone were mixed homogeneously to produce a uniform film on a glass substrate. The film was then put in vacuum for 10 min to remove air bubbles and placed in the air at room temperature for 12 h or at 60 °C for 2 h. Scanning electron microscope (SEM) images and energy-dispersive X-ray spectroscopy (EDX) mapping for $NaYGeO_4$:0.01Bi^{3+} were recorded with a JEOL JSM-IT100 instrument.

3. RESULTS

3.1. X-ray Diffraction and Photoluminescence Spectroscopy. Figure 2a shows the X-ray diffraction patterns (XRD) for the $NaYGeO_4$:0.01Bi^{3+} synthesized at 1200 °C during 3−24 h. All samples match well with the standard $NaYGeO_4$ reference (No. 2060220), indicating that high-purity samples were synthesized.

https://dx.doi.org/10.1021/acs.chemmater.9b04341
Chem. Mater. 2020, 32, 1192−1209

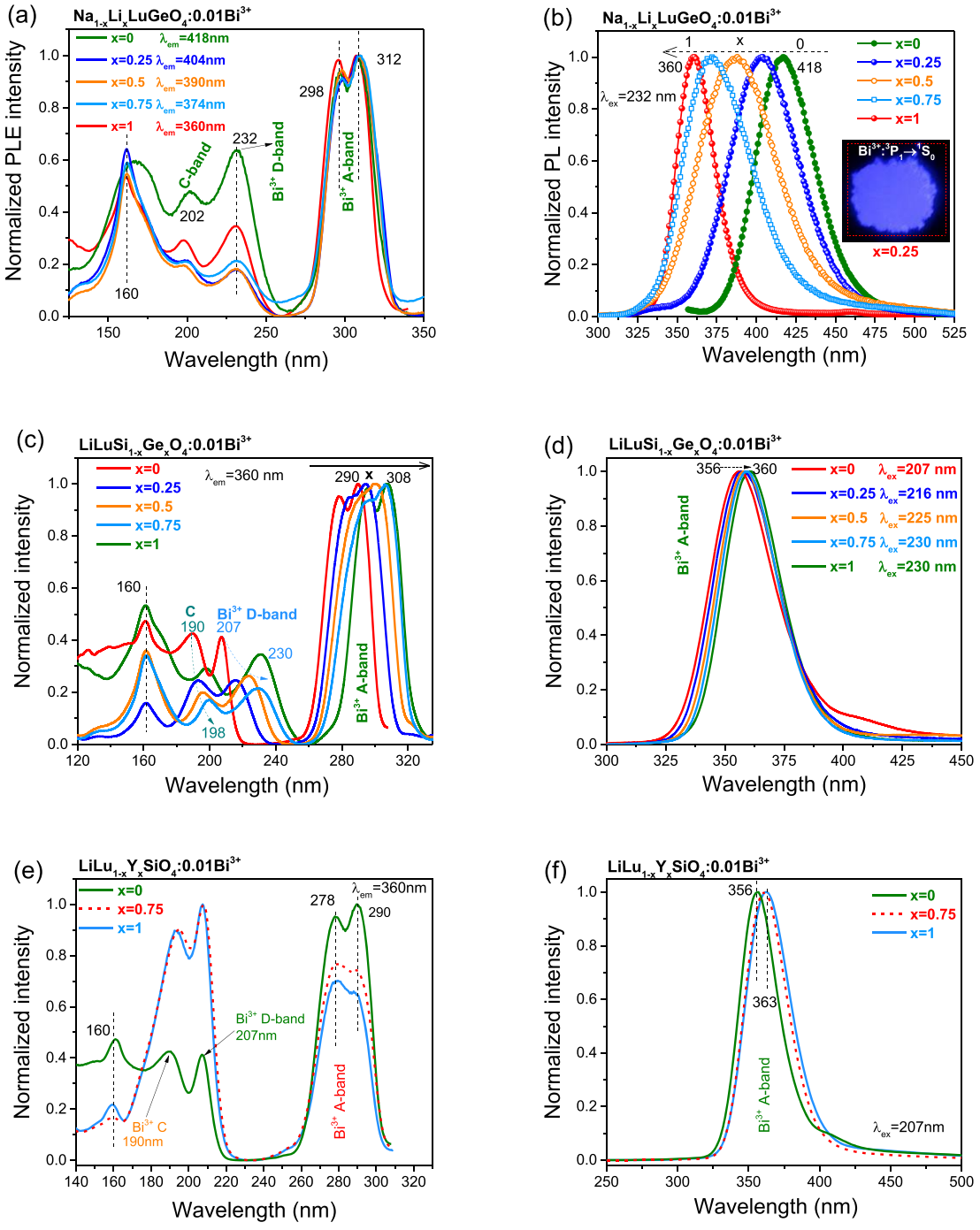

Figure 5. Photoluminescence excitation and emission spectra for (a, b) $Na_{1-x}Li_xLuGeO_4$: $0.01Bi^{3+}$, (c, d) $LiLuSi_{1-x}Ge_xO_4$:$0.01Bi^{3+}$, and (e, f) $LiLu_{1-x}Y_xSiO_4$:$0.01Bi^{3+}$ recorded at 10 K. An afterglow photograph of $Na_{1-x}Li_xLuGeO_4$:$0.01Bi^{3+}$ (x = 0.25) after Hg lamp irradiation for 5 s is shown in panel b. The shoulder emission band near 414 nm in panels d and f for $LiLuSiO_4$:$0.01Bi^{3+}$ is attributed to the second-order transmission of excitation light at 207 nm. This band is absent in other samples when a longer wavelength 305 nm pass filter is used.

Figure 2b shows part of the XRD patterns for $NaLu_{1-x}Y_xGeO_4$:$0.01Bi^{3+}$,$0.001Eu^{3+}$ with different content of Y^{3+}. Compared with the $NaLuGeO_4$ reference (No. 2060221), the XRD peaks slightly shift toward smaller 2θ angles. This demonstrates that the yttrium cations enter into the smaller lutetium site and increase the cell volume. With increasing x, nice solid solutions appear in the synthesized crystals of $NaLu_{1-x}Y_xGeO_4:0.01Bi^{3+}$, $0.0001Eu^{3+}$, $Na_{1-x}Li_xLuGeO_4$:$0.01Bi^{3+}$, or $LiLuSi_{1-x}Ge_xO_4$ (x = 0−1), where impurity phases are absent, as is evidenced with the X-ray diffraction patterns in Figure S2 of the Supporting Information (SI).

Figure 3a shows the excitation spectra for $LiLuSi_{1-x}Ge_xO_4$:$0.01Eu^{3+}$. A broad band near 225 nm is observed, which slightly shifts to ∼228 nm with increasing x. Like in the study of Sidorenko et al.,[48] this band is attributed to the charge transfer (CT) band, where an electron is excited from the valence band to Eu^{3+}, forming Eu^{2+} in its ground state.

Figure 3b,c shows the excitation and emission spectra of undoped $LiLuSi_{1-x}Ge_xO_4$ at 10 K. Several excitation peaks

https://dx.doi.org/10.1021/acs.chemmater.9b04341
Chem. Mater. 2020, 32, 1192−1209

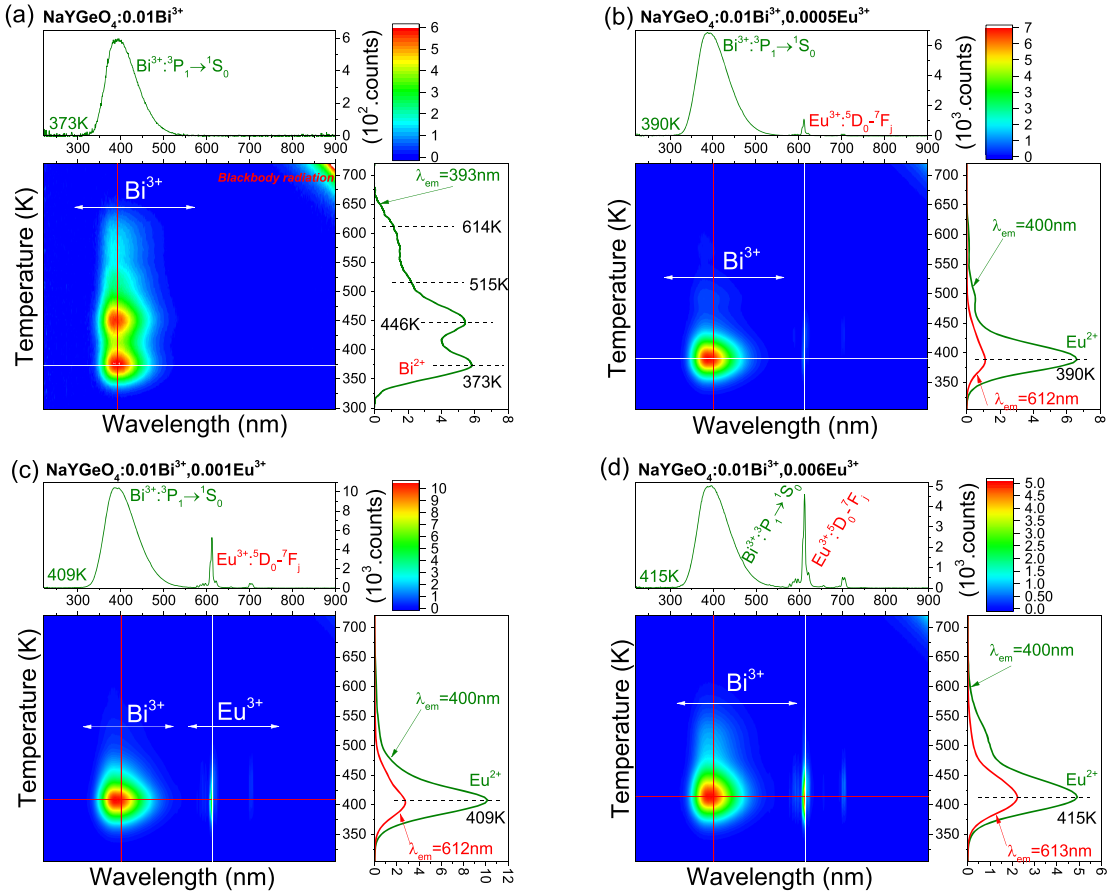

Figure 6. Thermoluminescence emission (TLEM) spectra for (a) $NaYGeO_4$:0.01Bi^{3+} synthesized at 1200 °C during 24 h, (b) $NaYGeO_4$:0.01Bi^{3+},0.0005Eu^{3+}, (c) $NaYGeO_4$:0.01Bi^{3+},0.001Eu^{3+}, and (d) $NaYGeO_4$:0.01Bi^{3+},0.006Eu^{3+} at β = 1 K/s after γ-ray irradiation.

near 179, 202, 238, and 316 nm appear. With increasing x, the excitation peaks do not exhibit a gradual shift, while the emission peaks near 320 and 422 nm shift toward lower energy.

Figure 4a,b show the photoluminescence excitation and emission for undoped or Bi^{3+} or Eu^{3+} single-activated $NaLuGeO_4$ crystals at 10 K. $NaLuGeO_4$:0.01Eu^{3+} shows 4f−4f emission upon 227 nm excitation, and its excitation spectrum monitoring at 612 nm gives rise to two excitation bands peaked at 227 and 196.5 nm. Like in the study of Blasse et al.,[49] the 227 nm band is known as a charge transfer (CT) band. When the host is excited at 198 nm, a broad emission band appears between 330 and 600 nm. Its excitation spectrum monitoring at 450 nm shows a strong excitation band near 196.5 nm that is the same as the one observed when monitored Eu^{3+} emission in $NaLuGeO_4$:0.01Eu^{3+}. This band near 196.5 nm will be assigned to host exciton creation.

When $NaLuGeO_4$:0.01Bi^{3+} is excited at 232 or 296 nm, a broad Bi^{3+} A-band emission with a maximum wavelength near 418 nm appears. Its excitation spectrum is composed of five bands near 166, 202, 232, 296, and 308 nm. Considering the Jahn−Teller splitting for the $^3P_1$ excited state for the s^2-type ions like Bi^{3+} and Tl^+,[37,50,51] the low-energy excitation bands located at 296 and 308 nm are, like in ref 41, attributed to the Jahn−Teller split $^1S_0 \rightarrow {}^3P_1$ transition. The assignment of the excitation band near 232 nm to the $Bi^{3+} \rightarrow$ CB (conduction band) charge transfer (CT) band, also known as the Bi^{3+} D-band, and the assignment of the 202 nm band to the C-band will be discussed in the Discussion section. Similar PLE and PL spectra for isostructural $NaYGeO_4$:0.01Bi^{3+} or -Eu^{3+} can be found in Figure S3 (SI).

Figure 4c,d shows the photoluminescence excitation spectra for Tb^{3+} or Pr^{3+} single-activated $NaLuGeO_4$, while monitoring the typical Tb^{3+} (548 nm) or Pr^{3+} (605 nm) emission as shown in Figure S5 (SI). A broad shoulder band near 258 nm appears for $NaLuGeO_4$:0.01Pr^{3+} in Figure 4c, 266 nm for $NaLuGeO_4$:0.005Tb^{3+} in Figure 4d, 260 nm for $LiLuGeO_4$:0.01Pr^{3+} in Figure S5a (SI), and 270 nm for $LiLuGeO_4$:0.01Tb^{3+} in Figure S5b (SI). The wavelength difference between that for Pr^{3+} and Tb^{3+} is ∼10 nm in both compounds. Similar PLE spectra for $NaYGeO_4$ can be found in Figure S5g,h (SI). In the Discussion section, these peaks are assigned to Intervalence Charge Transfer Bands (IVCT)[43] caused by electron transfer from the Tb^{3+} or Pr^{3+} 4f ground state to the conduction band.

To further reveal the nature of Bi^{3+} emission, Figure 5a,b shows the excitation and emission spectra of $Na_{1-x}Li_xLuGeO_4$:0.01Bi^{3+} solid solutions at 10 K. With increasing x, all excitation bands remain stationary, while the Bi^{3+} emission peak wavelength decreases gradually from 418 nm for x = 0 to 360 nm for x = 1 upon Bi^{3+} D-band excitation. The same applies to the emission bands when excited by the Bi^{3+} A-band at 308 nm, as shown in Figure S4 (SI).

Figure 5c,d shows the excitation and emission spectra for $LiLuSi_{1-x}Ge_xO_4$:0.01Bi^{3+} solid solutions at 10 K. The excitation peak near 160 nm remains stationary with increasing x, while a gradual red-shift appears in the Bi^{3+} A-,

https://dx.doi.org/10.1021/acs.chemmater.9b04341
Chem. Mater. 2020, 32, 1192−1209

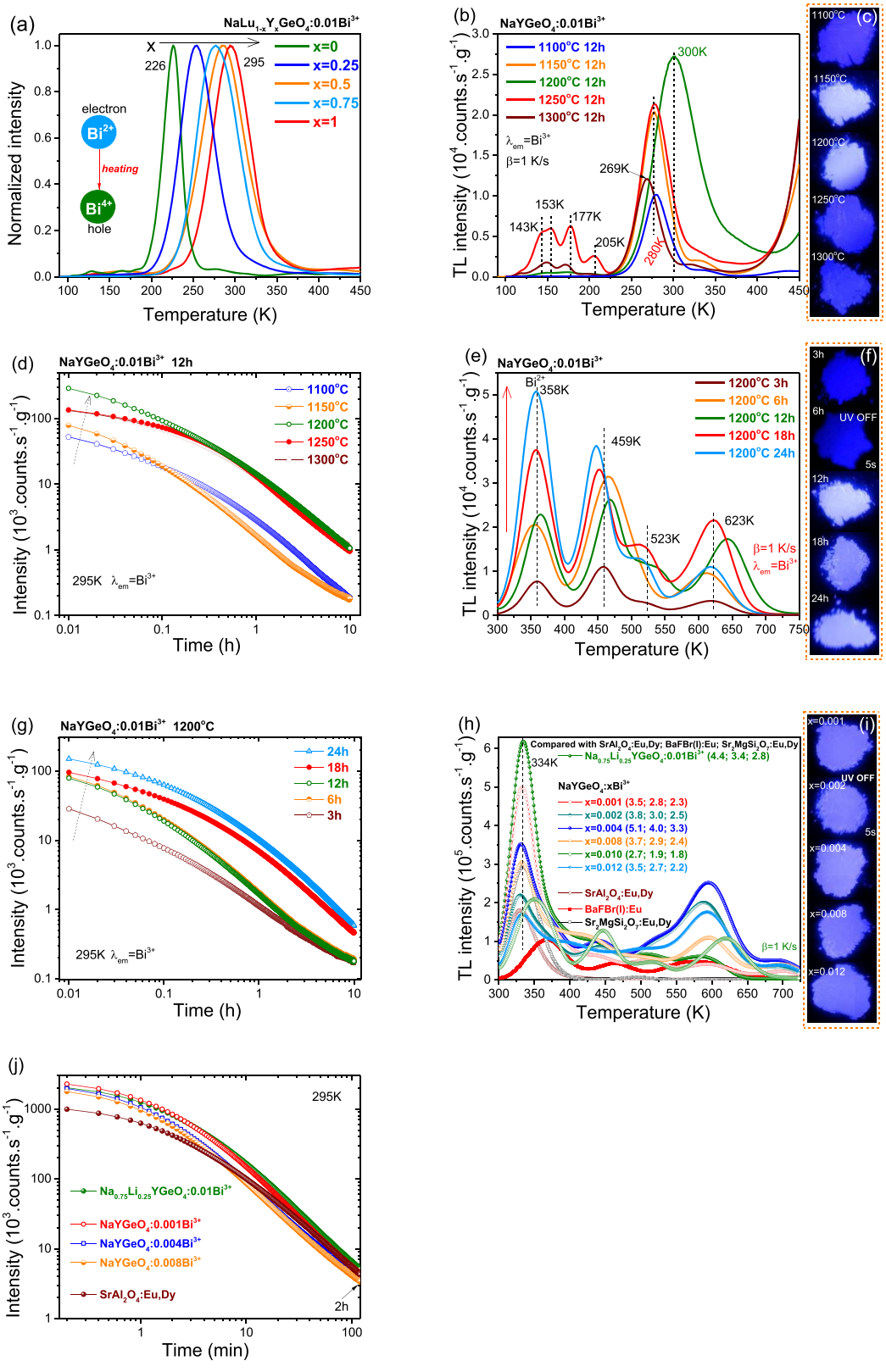

Figure 7. (a) Low-temperature TL glow curves at β = 1 K/s monitoring Bi^{3+} emission for $NaLu_{1-x}Y_xGeO_4$:0.01Bi^{3+} after β-irradiation. TL glow curves, photographs after Hg lamp irradiation for 5 s, and RT isothermal decay curves for $NaYGeO_4$:0.01Bi^{3+} synthesized at (b−d) different temperature, (e−g) at 1200 °C with different duration time, and (h−j) $NaYGeO_4$:xBi^{3+} and $Na_{0.75}Li_{0.25}YGeO_4$:0.01Bi^{3+} synthesized at 1200 °C during 24 h.

C-, and D- excitation bands and Bi^{3+} A-emission band. The same applies to the double solid solutions $LiLu_{0.25}Y_{0.75}Si_{1-x}Ge_xO_4$:0.01$Bi^{3+}$ in Figure S6 (SI).

Figure 5e,f shows the PLE and PL spectra for $LiLu_{1-x}Y_xSiO_4$:0.01Bi^{3+} at 10 K. The excitation peak near 160 nm, Bi^{3+} C-band near 190 nm, D-band near 207 nm, and

https://dx.doi.org/10.1021/acs.chemmater.9b04341
Chem. Mater. 2020, 32, 1192−1209

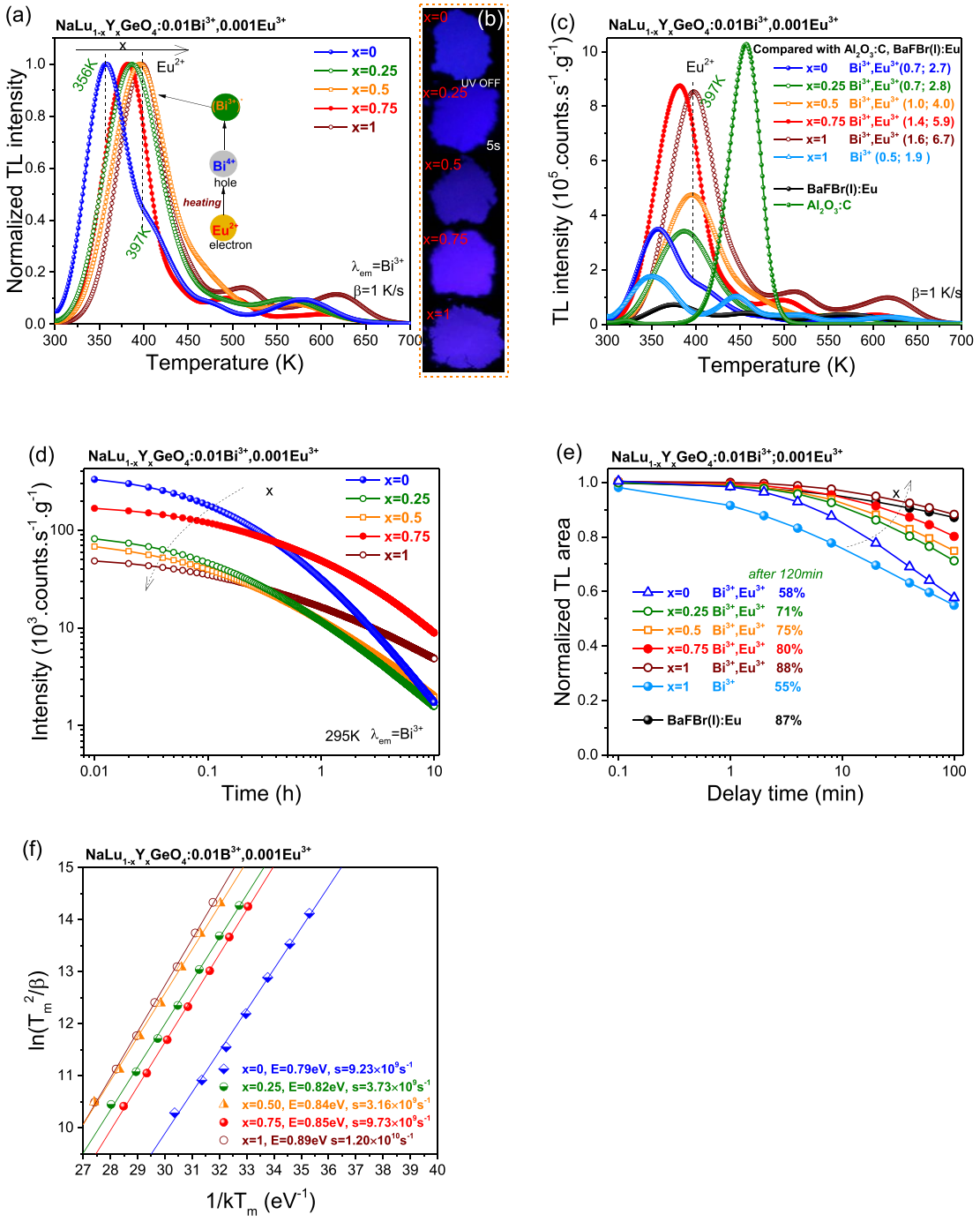

Figure 8. (a, c) TL glow curves at β = 1 K/s monitoring Bi^{3+} emission, (b) photographs after Hg lamp irradiation for 5 s, (d) RT isothermal decay curves, (e) TL fading characteristics, and (f) variable heating rate plots for $NaLu_{1-x}Y_xGeO_4$:0.01Bi^{3+},0.001Eu^{3+}. The applied heating rates were 0.08, 0.15, 0.3, 0.63, 1.25, 2.5, and 5 K/s.

A-bands near 278 and 290 nm remain stationary. A red-shift of about 7 nm appears in the Bi^{3+} A-band emission with increasing *x*. Note that the 160 nm excitation band is an artefact due to the deuterium lamp spectrum correction.

3.2. Engineering the Electron Trap Depth of Bi^{3+} and Eu^{3+} and Crystal Synthesis Optimization. TL emission (TLEM) studies were performed to identify the recombination center in Bi^{3+}-doped or Bi^{3+},Eu^{3+}-codoped $NaYGeO_4$ crystals, as shown in Figure 6. Additional TLEM plots for other $NaLu_{1-x}Y_xGeO_4$ with different Eu^{3+} concentration or Y^{3+} content can be found in Figure S9 (SI). For $NaYGeO_4$:0.01Bi^{3+}, TL peaks near 373, 446, 515, and 614 K with broad Bi^{3+} A-band emission peaked at ~400 nm appear. After codoping Eu^{3+} in $NaYGeO_4$:0.01Bi^{3+},0.001Eu^{3+} (Figure 6b), an about 10 times stronger Bi^{3+} TL peak near 390 K emerges. Not only typical Bi^{3+} A-band emission but also weak Eu^{3+} 4f−4f emission is observed. This is attributed to Bi^{3+} → Eu^{3+} energy transfer, because the TL peaks when monitoring the Eu^{3+} 4f−4f emission or when monitoring the Bi^{3+} A-band emission appear to share the same shape. This applies to $NaYGeO_4$:0.01Bi^{3+},0.001Eu^{3+} in Figure 6c, $NaYGeO_4$:0.01Bi^{3+},0.006Eu^{3+} in Figure 6d, and also to other

https://dx.doi.org/10.1021/acs.chemmater.9b04341
Chem. Mater. 2020, 32, 1192−1209

$NaLu_{1-x}Y_xGeO_4$:0.01Bi^{3+},xEu^{3+} in Figure S9 (SI). Note that the ratio of Eu^{3+} 4f−4f emission to Bi^{3+} A-band emission increases from 0.02 to 0.12 with increasing x in Figure 6b−d.

Figure 1a shows that the VRBE in the ground state of Eu^{2+} and Bi^{2+} appears near −4.0 and −3.5 ± 0.5 eV, respectively. It suggests that Bi^{3+} acts as a 0.5 ± 0.5 eV shallower electron trap than Eu^{3+} in $NaYGeO_4$. Bi^{3+} single-doped $NaLu_{1-x}Y_xGeO_4$ samples were synthesized to study the charge-carrier-trapping process. Figure 7a shows the low-temperature TL glow curves for $NaLu_{1-x}Y_xGeO_4$:0.01Bi^{3+} solid solutions. With increasing x, the TL glow near 226 K, which will be attributed to electron liberation from Bi^{2+}, shifts ∼69 K toward higher temperature.

Since the TL peak for $NaYGeO_4$:0.01Bi^{3+} is near 300 K in Figure 7a), persistent luminescence of Bi^{3+} is expected at RT. To optimize the charge carrier storage capacity to obtain stronger Bi^{3+} afterglow, synthesis optimization is explored. Figure 7b shows that the TL peak maximum changes between 269 and 300 K, depending on the synthesis temperature at 1100−1300 °C. Note that a ∼4.8 times stronger TL peak near 300 K appears when the synthesis temperature is increased from 1100 to 1200 °C. The stronger Bi^{3+} afterglow is evidenced by the photographs in Figure 7c and the RT isothermal decay curves in Figure 7d. Figure 7e,f shows the TL glow curves and photographs for $NaYGeO_4$:0.01Bi^{3+} synthesized at 1200 °C with different duration time. An about 7 times stronger Bi^{2+} TL peak near 358 K appears with increasing the duration time from 3 to 24 h, which results in stronger Bi^{3+} afterglow, as shown in Figure 7g. For the $NaYGeO_4$:0.01Bi^{3+} sample synthesized at 1200 °C during 12 h, the Bi^{2+} peak near 358 K in Figure 7e is ∼58 K higher than the Bi^{2+} peak near 300 K in Figure 7b. In the above RT TL experiment, a large part of the TL glow has already faded at the start of the recording. The 58 K shift is therefore attributed to a peak cleaning effect at RT, as is further demonstrated in Figure S10 (SI).

Figure 7h,i shows the TL glow curves and photographs for $NaYGeO_4$:xBi^{3+} and $Na_{0.75}Li_{0.25}YGeO_4$:0.01Bi^{3+} samples synthesized at 1200 °C during 24 h. The TL glow near 300−400 K appears to increase ∼2.5 times when x changes from 0.01 to 0.001 or when 25% Na^+ is replaced by Li^+, which results in strong Bi^{3+} afterglow in Figure 7j. The ratios of integrated TL between 300 and 723 K of $NaYGeO_4$:xBi^{3+} and $Na_{0.75}Li_{0.25}YGeO_4$:0.01Bi^{3+} to that of commercial phosphors $SrAl_2O_4$:Eu,Dy (G-300M, LumiNova), BaFBr(I):Eu (Agfa-Gevaert), and $Sr_2MgSi_2O_7$:Eu,Dy are provided in the legend of Figure 7h.

Figure 1a suggests that Eu^{3+} may act as a ∼0.5 ± 0.5 eV deeper electron trap than Bi^{3+}. The storage phosphor properties of Bi^{3+},Eu^{3+}-codoped $NaLu_{1-x}Y_xGeO_4$ solid solutions were therefore explored. Figure 8a,c show the normalized and unnormalized TL glow curves for $NaLu_{1-x}Y_xGeO_4$:0.01Bi^{3+},0.001Eu^{3+} after β-irradiation. The ratios of integrated TL between 300 and 700 K of $NaLu_{1-x}Y_xGeO_4$:0.01Bi^{3+},0.001Eu^{3+} to that of commercial storage phosphor BaFBr(I):Eu or a Al_2O_3:C single crystal (Landauer Inc.) are shown in the legend of Figure 8c. The maximal ratios of 6.7 and 1.6 appear when x = 1. With increasing x, the TL glow peak attributed to electron release from Eu^{2+} near 356 K shifts ∼41 K toward higher temperature in Figure 8c, which gives rise to decreased initial Bi^{3+} afterglow in Figure 8d and less TL fading in Figure 8e. For the x = 1 phosphor after 2 h waiting time, the integrated TL intensity remains 88%, which is almost the same as that of BaFBr(I):Eu (87%). Note that the Eu^{2+} TL peak temperature of 397 K in Figure 8c for the x = 1 phosphor is about 12 K lower than that of the Eu^{2+} TL peak in Figure 6c. In the TLEM experiments in Figure 6, there is about 0.5 h delay time between γ-ray charging and TL recording, and a small part of the Eu^{2+} TL glow has already faded at RT before the start of TL recording.

The trapping depths for $NaLu_{1-x}Y_xGeO_4$:0.01Bi^{3+},0.001Eu^{3+} were determined by utilizing a variable heating rate plot and equation:[19,52−54]

$$\ln\left(\frac{T_m^{\,2}}{\beta}\right) = \frac{E}{kT_m} + \ln\left(\frac{E}{ks}\right) \quad (1)$$

where β is the heating rate, which can change from 0.08 to 5 K/s; T_m is the temperature at the maximum of the TL glow curve; k represents the Boltzmann constant (8.62×10^{-5} eV/K); and s stands for the frequency factor (s^{-1}). Figure 8f shows the variable heating rate plots for $NaLu_{1-x}Y_xGeO_4$:0.01Bi^{3+},0.001Eu^{3+} that provide the trap depths shown in column 4 and the frequency factors in column 2 of Table 1.

Table 1. TL Results for Solid Solutions $NaLu_{1-x}Y_xGeO_4$:0.01Bi^{3+} and $NaLu_{1-x}Y_xGeO_4$:0.01Bi^{3+},0.001Eu^{3+} Giving the Frequency Factor s (s^{-1}) and Trapping Depths E (eV) for the Eu^{2+} and Bi^{2+} Glow Peaks (T_m)

x	s	T_m Eu^{2+} (K)	Eu E (eV)	T_m Bi^{2+} (K)	Bi E (eV)
0	9.23×10^9	356	0.79	226	0.49
0.25	3.73×10^9	386	0.82	254	0.53
0.50	3.16×10^9	394	0.84	285	0.59
0.75	9.73×10^9	382	0.85	277	0.61
1	1.20×10^{10}	397	0.89	295	0.65

Because the Eu^{3+} content is very low, we assumed that the above-derived s values also apply to $NaLu_{1-x}Y_xGeO_4$:0.01Bi^{3+}. Assuming a first-order TL recombination kinetic, the corresponding trapping depths E (eV) for the Bi^{2+} TL peaks in $NaLu_{1-x}Y_xGeO_4$:0.01Bi^{3+} in Figure 7a can then be derived by using the temperature T_m at the maximum of the TL glow curve and solving eq 1 with β = 1 K/s and s values in column 2. The obtained results are provided in column 6 of Table 1. Actually, first-order kinetics does not apply, and one should regard the obtained values as indicative.

To further unravel the charge-carrier-trapping processes regarding Bi^{3+}, Figure 9a,b shows the TL excitation (TLE) plots for Bi^{3+}-doped and Bi^{3+},Eu^{3+}-codoped $NaYGeO_4$. Additional TLE plots under other synthesis conditions or Eu^{3+} concentrations for $NaLu_{1-x}Y_xGeO_4$ are given in Figure S15 (SI). All traps corresponding with the TL peaks near 383 K (from Bi^{2+}), 492, 562, or 666 K in Figure 9a or the Eu^{2+} TL peak near 422 K in Figure 9b can be charged by photons near 230 nm. A comparison of TLE plots with photoluminescence spectra is shown in Figure 9c. For all samples, a broad thermoluminescence excitation band peaked at about 230 nm and ranging between 200 and 270 nm appears in Figure 9c3−c11). Its width and peak position overlap with those of the Bi^{3+} D-band in Figure 9c1 or the VB → Eu^{3+} CT-band in Figure 9c2.

https://dx.doi.org/10.1021/acs.chemmater.9b04341
Chem. Mater. 2020, 32, 1192−1209

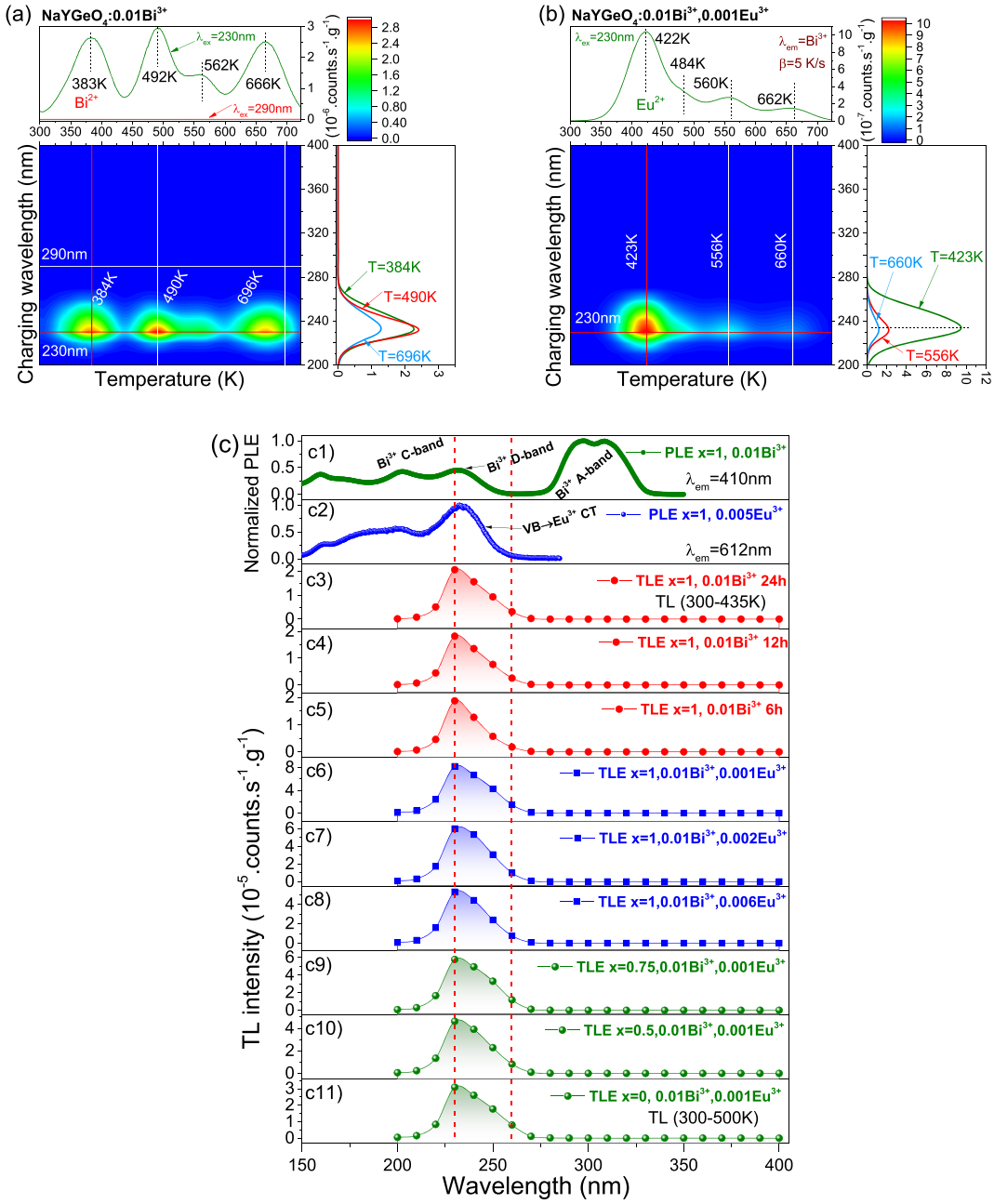

Figure 9. TL excitation (TLE) plots at β = 5 K/s while monitoring the Bi^{3+} emission for (a) $NaYGeO_4$:0.01Bi^{3+} synthesized at 1200 °C during 24 h, (b) $NaYGeO_4$:0.01Bi^{3+},0.001Eu^{3+}, and (c) $NaLu_{1-x}Y_xGeO_4$:0.01Bi^{3+},0.001Eu^{3+}. The TL glow peak between 300 and 435 K in panel a was integrated to establish the TLE plots in panels c3−c5, and for panels c6−c11, the TL glow peak between 300 and 500 K in panel b was integrated. Panels c1 and c2 show the photoluminescence excitation spectra for $NaYGeO_4$:0.01Bi^{3+} at 10 K and $NaYGeO_4$:0.005Eu^{3+} at RT, respectively.

3.3. Evaluating the Potential Applications for Information Storage. Figure 10 shows the TL glow curves for $NaYGeO_4$:0.01Bi^{3+}, $NaYGeO_4$:0.01Bi^{3+},0.001Eu^{3+}, and BaFBr(I):Eu. After exposure to water for 0.5 h, the TL intensity of BaFBr(I):Eu almost completely disappeared. The integrated TL intensity remains 69% for $NaYGeO_4$:0.01Bi^{3+},0.001Eu^{3+}, 56% for $NaYGeO_4$:0.01Bi^{3+}, 7% for BaFBr(I):Eu, and 81% for $NaLu_{0.25}Y_{0.75}GeO_4$:0.01Bi^{3+},0.001Eu^{3+} in Figure S16a (SI).

The stored information is usually read out using a stimulating photon beam. For comparison with commercial phosphors, Figure 11 shows part of the TL glow curves after optical stimulation. Additional plots for other $NaLu_{1-x}Y_xGeO_4$ are shown in Figure S18 (SI).

Figures 11 and S18 (SI) show that 10 s of 475 nm LED stimulation liberates ~27, 14, 57, 56, 95, and 41% of the stored charge carriers during β-ray irradiation for $NaYGeO_4$:0.01Bi^{3+}, $NaYGeO_4$:0.01Bi^{3+},0.001Eu^{3+}, $NaYGeO_4$:0.01Bi^{3+},0.002Eu^{3+}, $NaY_{0.75}Lu_{0.25}GeO_4$:0.01Bi^{3+}, 0.001Eu^{3+}, BaFBr(I):Eu, and Al_2O_3:C, respectively. Note that the relative amount of liberated charge carriers is smaller, but the absolute amount is about 2 and 4 times higher in $NaYGeO_4$:0.01Bi^{3+},0.002Eu^{3+} and $NaY_{0.75}Lu_{0.25}GeO_4$:0.01Bi^{3+},0.001Eu^{3+} than that in BaFBr(I):Eu and Al_2O_3:C, respectively. This means that a lower

https://dx.doi.org/10.1021/acs.chemmater.9b04341
Chem. Mater. 2020, 32, 1192−1209

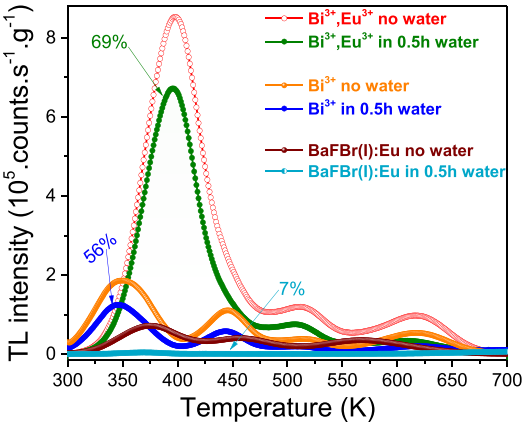

Figure 10. TL glow curves at β = 1 K/s for $NaYGeO_4$:0.01Bi^{3+}, $NaYGeO_4$:0.01Bi^{3+},0.001Eu^{3+}, and BaFBr(I):Eu after exposure to water after β-irradiation.

dose can be used to arrive at the same signal, which is beneficial for patients. Figure S18a,b (SI) shows that charge carriers liberated between 300 and 425 K are partly transferred to the deeper traps.

Figure 11a,b demonstrates that about 95% of stored information can be erased by increasing the stimulation time to 1200 s, indicating potential use as optically stimulated storage phosphors. BaFBr(I):Eu is erased much more efficiently at 475 nm.

To add security features for anti-counterfeiting applications, we explored tailoring of the afterglow color. Figure 12a1−a4 shows that $CsPbBr_3$ and CdSe quantum dots (QDs) have green or red photoluminescence but no afterglow. Red emission due to an energy transfer from $NaYGeO_4$:0.01Bi^{3+} afterglow to QDs appears in film 1 in Figure 12b3, which is composed of $NaYGeO_4$:0.01Bi^{3+} and $CsPbBr_3$ and CdSe QDs. The afterglow spectrum for film 1 in Figure S22a (SI) shows that the emission from CdSe QDs is stronger than that from $CsPbBr_3$ QDs and from the Bi^{3+} A-band, resulting in the red color. Cyan afterglow appears in film 2 in Figure 12c3, where the ratio of CdSe to $CsPbBr_3$ is lower than that in film 1. Figure 12b4,b5,c4) shows that text can be clearly displayed using the red and cyan afterglow.

A QR code was generated by computer software using the text of "No.000000X1; Delft University of Technology; 18−06−2019" and "TUD" as shown in Figure 12c5,d1). One may print the QR code in Figure 12d1 using an afterglow $NaYGeO_4$:0.01Bi^{3+} phosphor. This QR code appears in the dark in Figure 12d2 due to Bi^{3+} afterglow, which has potential anti-counterfeiting application on paper like bank notes.

A paper printed with a QR code using black ink in Figure 12c5 is visible in the dark in Figure 12c6 due to the cyan afterglow from film 2 underneath the paper in Figure 12c3. The QR code can be scanned in the dark with smart phone software to read out the hidden text information of "No.000000X1; Delft University of Technology; 18−06−2019", as shown in Figure 12c7.

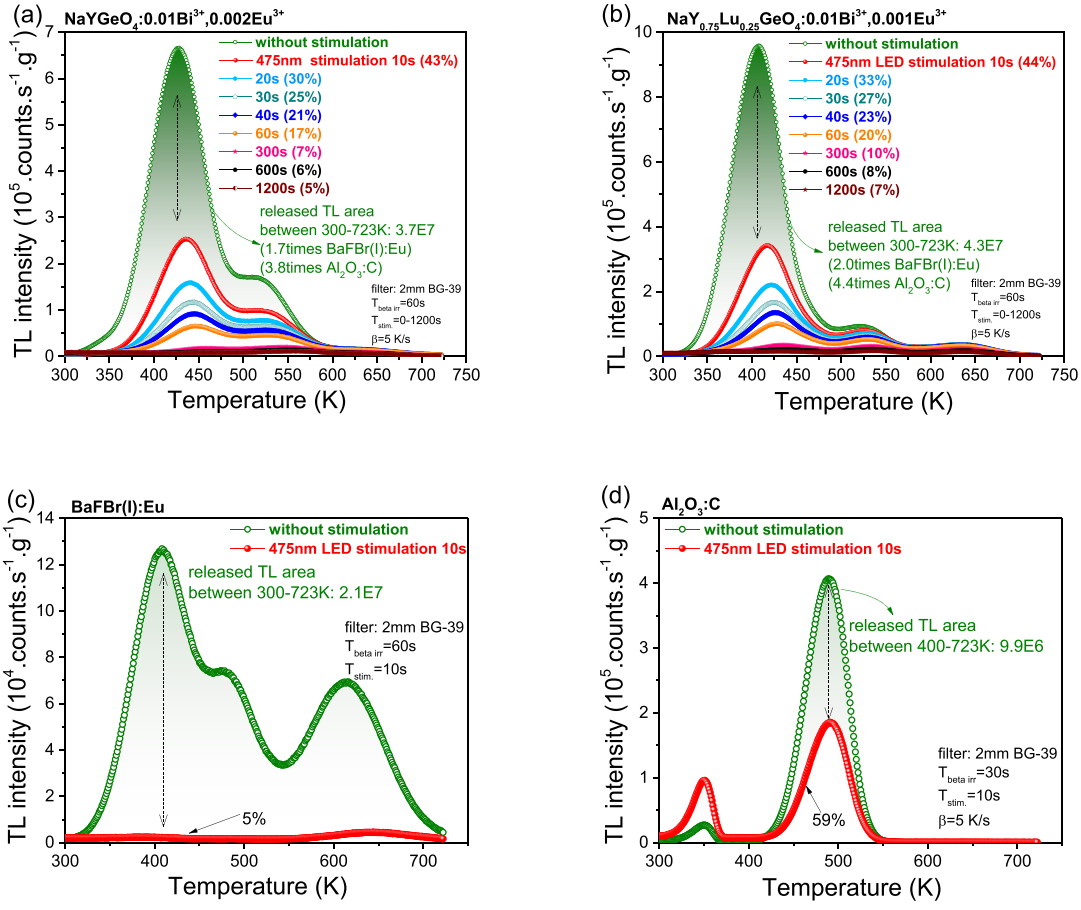

Figure 11. TL glow curves at β = 5 K/s for (a) $NaYGeO_4$:0.01Bi^{3+},0.002Eu^{3+}, (b) $NaY_{0.75}$ $Lu_{0.25}GeO_4$:0.01B^{3+},0.001Eu^{3+}, (c) BaFBr(I):Eu, and (d) Al_2O_3:C single crystal measured after β-irradiation and after β-irradiation followed by 475 nm LED optical stimulation with different duration.

https://dx.doi.org/10.1021/acs.chemmater.9b04341
Chem. Mater. 2020, 32, 1192−1209

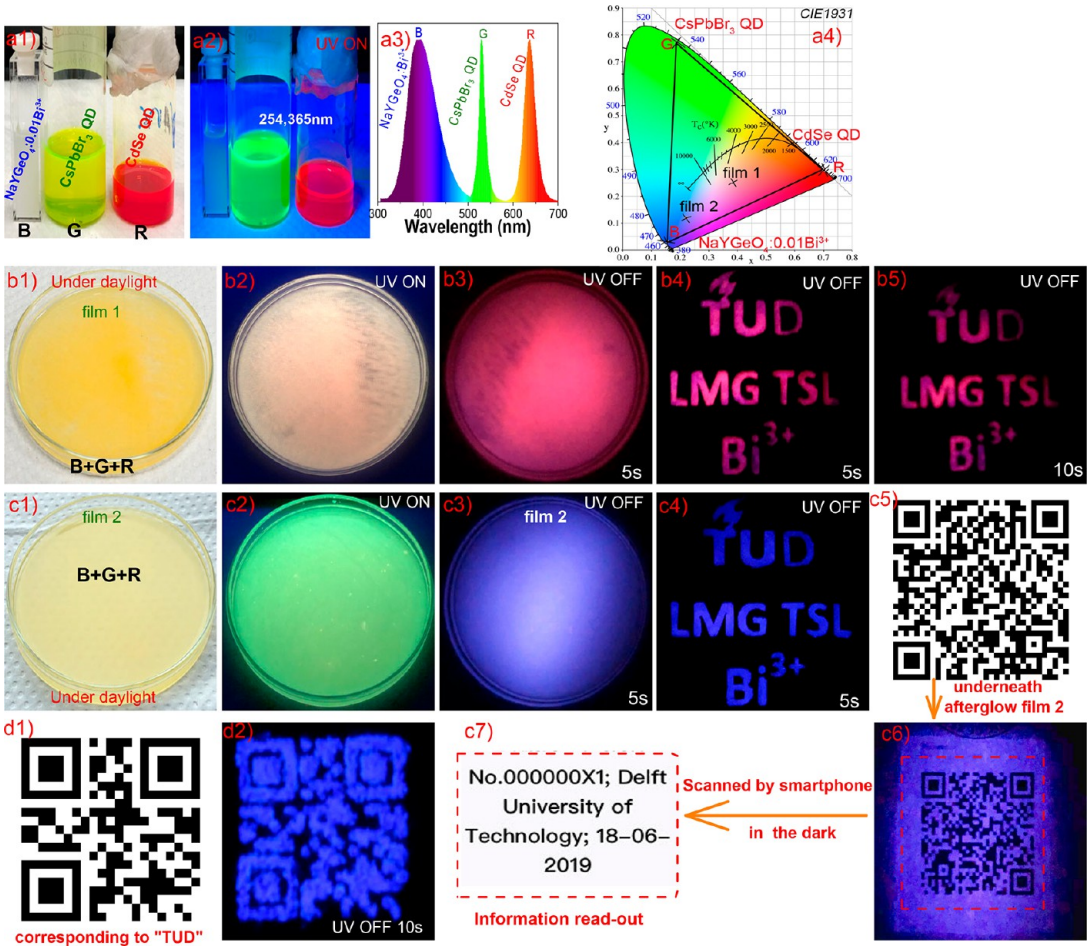

Figure 12. Proof-of-concept color tuning for anti-counterfeiting applications by combining an afterglow film with quantum dot (QD) phosphors. Photographs of $NaYGeO_4$:0.01Bi^{3+} and $CsPbBr_3$ and CdSe QDs under (a1) daylight and (a2) UV light and (a3) the corresponding PL spectra and (a4) color coordinates. Panels b1−b5 show the CdSe-QD-rich afterglow film 1 and its application to display texts. Panels c1−c7 show the $CsPbBr_3$-QD-rich film 2 and its application to display texts or a QR code on paper in the dark. Panels d1 and d2 show Bi^{3+} afterglow from $NaYGeO_4$:0.01Bi^{3+} to display a QR code in the dark.

$NaYGeO_4$:0.01Bi^{3+},0.001Eu^{3+} phosphor dispersed in a silicone gel film in Figure 13a1 is placed underneath a black mask in Figure 13a2. The text of "TUD LMG TSL Bi^{3+}" is stored when the 254 nm UV light goes through the empty area of the mask and charges the film. The text is visible due to Bi^{3+} afterglow in the dark in Figure 13a3. The Bi^{3+} afterglow intensity from $NaYGeO_4$:0.01Bi^{3+},0.001Eu^{3+} decreases rapidly and the text is invisible 60 s after switching the UV off. However, after the UV is off for 1 h, the text appears again in Figure 13a5,a6 due to thermally stimulated Bi^{3+} emission upon heating to ∼380 K. The process similarly applies to an X-ray image of a chicken bone stored in the film, as shown in Figure 13b1−b6. The thermally stimulated Bi^{3+} emission near 380 K in the rectangle area in Figure 13b3−b6 is weak because a large part of X-rays has been absorbed by the chicken bone during X-ray exposure.

4. DISCUSSION

We will first address the photoluminescence spectroscopy regarding the bismuth- and lanthanides-activated ARE(Si,Ge)O_4 (A = Li, Na; RE = Y, Lu). Then, the results are used to establish the so-called vacuum-referred binding energy (VRBE) diagrams, which enable us to compare the binding energy of an electron in impurity defects like Bi^{3+}, Bi^{2+}, or divalent and trivalent lanthanides within the band gap for different compounds with respect to the vacuum energy reference. Finally, we will show how to explore and explain the Bi^{3+} persistent luminescence and storage phosphors using the crystal synthesis optimization in $NaLu_{1-x}Y_xGeO_4$ based on the constructed VRBE schemes.

4.1. Vacuum-Referred Binding Energy Diagrams of ARE(Si,Ge)O_4 (A = Li, Na; RE = Y, Lu). Figure 3a shows the excitation spectra for $LiLuSi_{1-x}Ge_xO_4$:0.01Eu^{3+} at 10 K. The peaks near 167 nm appear to be the same with increasing x. The same applies to the excitation peak near 160 nm in Figure 5, which is all attributed to an artefact from the deuterium lamp correction. The Eu^{3+} charge transfer (CT) energy is known as the energy to excite an electron from the valence band top to Eu^{3+}, generating Eu^{2+} in its $4f^7$ ground state.[55] The VRBE in the Eu^{2+} ground state is always near −4 eV for oxide compounds.[56] It means that the Eu^{3+} CT-band energy provides direct information about the position of the valence band top. Figure 3a shows that the Eu^{3+} CT-band near 5.56 eV for x = 0 slightly shifts to 5.44 eV for x = 1. Considering the Eu^{3+} CT energy lowering in $LiLuSi_{1-x}Ge_xO_4$, the valence band top increases by ∼0.12 eV with increasing x from 0 to 1. The Eu^{3+} CT-band is near 5.49 eV for $NaLuGeO_4$ in Figure 4a and 5.46 eV for $NaYGeO_4$ in Figure S3 (SI). It means that

https://dx.doi.org/10.1021/acs.chemmater.9b04341
Chem. Mater. 2020, 32, 1192−1209

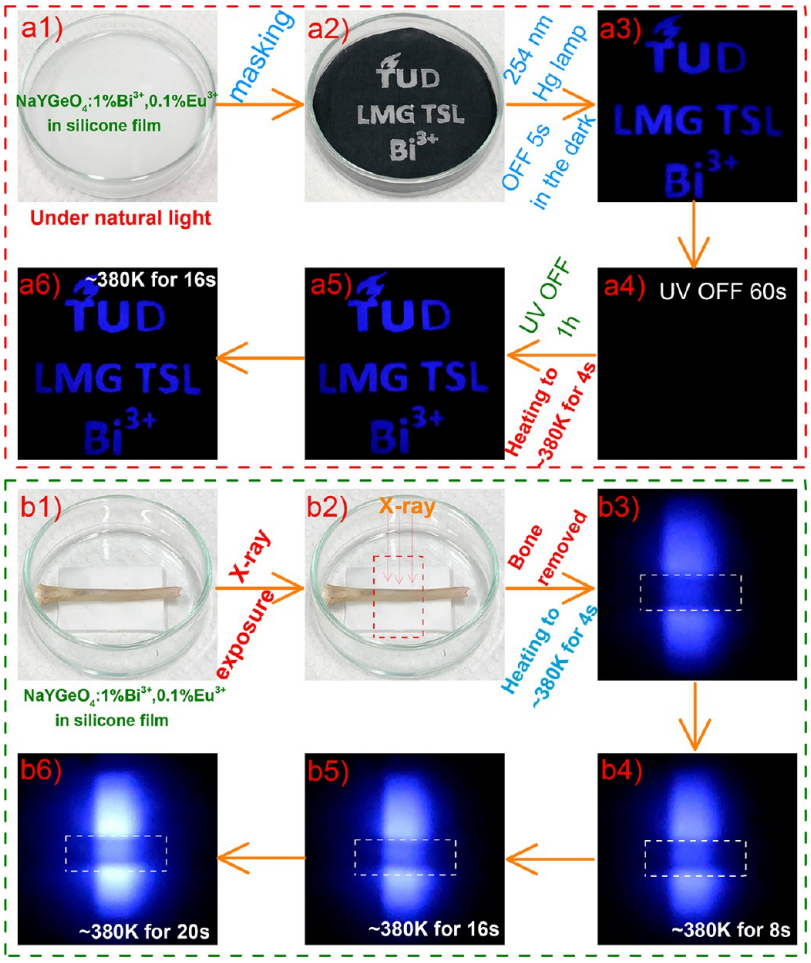

Figure 13. Proof-of-concept information storage using $NaYGeO_4$:0.01Bi^{3+},0.001Eu^{3+} phosphor dispersed in a silicone gel film. Information storage and display of text of "TUD LMG TSL Bi^{3+}" in panels a1−a6 and of an X-ray image of a chicken bone in panels b1−b6 are demonstrated. The chicken bone was removed before heating in panels b3−b6 and the mask was not removed in panels a3−a6. The white rectangle dash line is drawn to guide eyes.

the VB top VRBE of $NaLuGeO_4$ or $NaYGeO_4$ is similar to that of $LiLuGeO_4$. Considering that CT-band energies are not more accurate than ±0.1 eV, the VRBE at the VB top for all compounds studied are almost the same. Slight (<0.1 eV) differences can only be revealed by a changing T_m of glow peaks.

Figure 3b,c shows the PL excitation and emission spectra for undoped $LiLuSi_{1-x}Ge_xO_4$ at 10 K. The excitation and emission features are associated with unknown host intrinsic defect(s), and the host exciton creation energies for $LiLuSiO_4$ and $LiLuGeO_4$ cannot be determined with these excitation spectra. From previous work in refs 48 and 57, the host exciton creation is known to occur near 7.45 eV (166 nm) for $LiLuSiO_4$. Note that a host exciton creation band is absent in the excitation spectrum of $LiLuSiO_4$ in Figure 3b, implying inefficient energy transfer from the host exciton to the intrinsic defect(s).

Figure 4a shows the excitation spectra for undoped and Eu^{3+} and Bi^{3+} single-doped $NaLuGeO_4$ at 10 K. The excitation peak near 196.5 nm is common to the undoped and Eu^{3+}-doped $NaLuGeO_4$ and is attributed to the host exciton creation. For $NaYGeO_4$:0.01Eu^{3+} in Figure S3a (SI), a similar peak near 195 nm appears, indicating that the band gap of $NaLuGeO_4$ is ~0.05 ± 0.1 eV smaller than that of $NaYGeO_4$. The band-to-band excitation not only generates excitons but also yields emission from host intrinsic defects or dopants like Eu^{3+} in Figure 4b via excitation energy transfer from the host exciton. Note that a dip near 190 nm appears in the excitation spectrum for $NaLuGeO_4$:0.01Bi^{3+} in Figure 4a. It means that energy transfer from the exciton to Bi^{3+} is much less efficient than that from exciton to Eu^{3+}.

The electron transfer from the Tb^{3+} or Pr^{3+} 4f ground state to the conduction band (CB) was also explored. This transition is known as the intervalence charge transfer (IVCT),[43,58,59] which is often observed when the lowest 5d level is higher than the CB bottom, like in $LuNbO_4$.[60] IVCT gives information about the position of the conduction band with respect to the Pr and Tb ground states. The germanium-based compounds often have a low-lying conduction band, like in $(Sr,Ca)_3(Y,Lu)_2Ge_3O_{12}$, which leads to a low Ce^{3+} emission quenching temperature.[56] For Ce-doped $NaLuGeO_4$, we observed very weak emission only at 10 K (data not presented here). This means that the relaxed Ce^{3+} 5d level is close below the conduction band bottom and emission from Ce^{3+} 5d-4f is quenched above 10 K. Since the 5d level of Tb^{3+} and Pr^{3+} is at about the same VRBE as that of Ce^{3+}, they are also close to the CB bottom. This also implies that the Tb^{3+} → CB or Pr^{3+} → CB IVCT-bands may be observed in $NaLuGeO_4$.

https://dx.doi.org/10.1021/acs.chemmater.9b04341
Chem. Mater. 2020, 32, 1192−1209

Table 2. Parameters and Data Utilized To Construct the VRBE Schemes of the $NaYGeO_4$-Related Compound Family (in eV) and Level Energies Determined from These Schemes

compound	U	$E_{Eu^{2+}}$	$E_{Eu^{3+},CT}$	E_V	E^{ex}	E_C	$E_{Bi^{3+},CT}$	$E_{Bi^{3+}}$
$NaYGeO_4$	6.90	−4.02	5.46	−9.48	6.49	−2.65	5.35	−8.00
$NaLuGeO_4$	6.90	−4.02	5.49	−9.51	6.45	−2.72	5.34	−8.07
$LiLuGeO_4$	6.90	−4.02	5.44	−9.46	6.37	−2.76	5.37	−8.13
$LiLuSiO_4$	6.90	−4.02	5.56	−9.58	7.45	−1.69	5.99	−7.68
$LiYSiO_4$	6.90	−4.02	5.51	−9.53	7.55	−1.52	5.98	−7.50

Figure 4c,d shows the excitation spectra for Pr^{3+}- or Tb^{3+}-doped $NaLuGeO_4$. Three peaks near 207, 236, and 258 nm appear for $NaLuGeO_4$:0.01Pr^{3+} in Figure 4c. The excitation band near 207 nm is common for Pr^{3+}- or Tb^{3+}-doped samples that is likely associated with host exciton creation at RT. Considering the low-lying conduction band for $NaLuGeO_4$, the lowest energy 258 nm shoulder band is attributed to Pr^{3+} → CB IVCT and the higher energy band near 238 nm to Pr^{3+} 4f → 5d. The similar applies to $LiLuGeO_4$:0.01Pr^{3+} in Figure S5a (SI). About 10 nm longer wavelength bands near 266 nm for $NaLuGeO_4$:0.005Tb^{3+} in Figure 4d and near 270 nm for $LiLuGeO_4$:0.01Tb^{3+} in Figure S5b (SI) appear. In Tb^{3+}- or Pr^{3+}-doped $LuNbO_4$,[43] the band due to Tb^{3+} → CB IVCT is present at ∼10 nm longer wavelength than that of Pr^{3+} → CB IVCT. Here the bands near 266 and 270 nm are attributed to Tb^{3+} → CB IVCT.

For the method to establish VRBE schemes like in Figure 1 using spectroscopic data compiled in Table 2, we refer to refs 42, 44, and 46. For each compound, we used a U-value of 6.90 eV, which then determines the VRBE in the Eu^{2+} ground state but also for all other divalent and trivalent lanthanides. The $E_{Eu^{3+},CT}$ energy then defines E_V, and adding E^{ex} plus the exciton binding energy provides E_C. One may equally well add the IVCT band energies for Pr^{3+} and Tb^{3+} to their ground state energies to obtain E_C. In Table 2 we adopted energies for E_C that are consistent with both methods. It also supports the assignment of the excitation band near 195−205 nm in Ge-based $NaREGeO_4$ (RE = Y, Lu) compounds in Figures 4a and S3a (SI) to exciton creation. Note that our band gap E^{ex} near 6.3 eV and $E_{Eu^{3+},CT}$ energy 5.49 eV for $NaLuGeO_4$ are quite different from those used by Wang et al.[41] (4.4 eV and 3.77 eV).

Figure 4a shows the excitation spectrum for $NaLuGeO_4$:0.01Bi^{3+} at 10 K. An empirical equation regarding the relation between the Bi^{3+} A-band (E_A) and the C-band (E_{BiC}) was proposed as eq 2:[61]

$$E_{BiC} = 3.236 + 2.290(E_A - 2.972)^{0.856} \quad (2)$$

With the Bi^{3+} $^1S_0$ → $^3P_1$ A-band near 296 and 308 nm for $NaLuGeO_4$:0.01Bi^{3+}, the Bi^{3+} $^1S_0$ → $^1P_1$ C-band is then predicted to be near 208−220 nm. This value is close to the experimentally observed high-energy band near 202 nm, which is therefore attributed to the Bi^{3+} C-band. The relatively low-energy band near 232 nm is then assigned to the Bi^{3+} to CB charge transfer or D-band. It means that afterglow or storage phosphors can be charged via Bi^{3+} D-band excitation. This is consistent with the TL excitation spectra in Figure 9.

With the Bi^{3+} A-band near 278 and 290 nm for $LiLuSiO_4$:0.01Bi^{3+} in Figure 5e, the Bi^{3+} C-band is predicted by eq 2 to be near 192−203 nm, which resembles the experimental band near 190 nm. We therefore attribute the band near 190 nm to the Bi^{3+} C-band and the band near 207 nm to the Bi^{3+} D-band. Subtracting the Bi^{3+} D-band energies in column 8 from E_C, the VRBEs in Bi^{3+} $^1S_0$ ground states are obtained as listed in column 9 of Table 2. These values are consistent with ref 44. where the VRBE in the $^1S_0$ ground state of Bi^{3+} in a wide range of oxide compounds was found to be between −5 and −10 eV. A study by Awater et al.[45] showed that the VRBE in the Bi^{2+} $^2P_{1/2}$ ground state is near 3.5 ± 0.5 eV in oxide compounds. We assume that this Bi^{2+} value also applies to ARE(Si,Ge)O_4 (A = Li, Na; RE = Y, Lu) in this work. For $NaREGeO_4$ (RE = Y, Lu), the predicted VRBE in the Bi^{2+} ground state will be compared with the TL results in the next section.

Figure 5a,b shows the excitation and emission spectra for $Na_{1-x}Li_xLuGeO_4$:0.01Bi^{3+} solid solutions. With increasing x, the Bi^{3+} A-, C-, or D-excitation bands remain stationary, while the Bi^{3+} A-band emission gradually shifts from 418 to 360 nm. This means that more Li leads to weaker host lattice relaxation, resulting in emission of higher energy photons. A similar result emerges for $LiLu_{1-x}Y_xSiO_4$:0.01Bi^{3+} in Figure 5e,f, where an about 7 nm larger Stokes shift appears with increasing x. Apparently, replacing Lu by Y contributes to slightly stronger host lattice relaxation. For $LiLuSi_{1-x}Ge_xO_4$:0.01Bi^{3+} in Figure 5c,d, a ∼14 nm smaller Stokes shift appears. Considering the excitation band shifting, it is likely associated with the nephelauxetic effect when Si is replaced by Ge.

4.2. Designing Bi^{3+} Afterglow and Storage Phosphor via Conduction Band Engineering and Crystal Synthesis Optimization. The stacked VRBE diagram for $NaREGeO_4$ (RE = Y, Lu) in Figure 1a illustrates that Bi^{3+} will act as a ∼1.5 eV deep hole-capturing center, while Bi^{3+} and Eu^{3+} will act as ∼0.8 ± 0.5 and ∼1.3 eV deep electron-capturing centers in $NaLuGeO_4$. Electrons trapped to form Bi^{2+} or Eu^{2+} are then expected to be liberated at a lower temperature than holes captured at Bi^{4+} to generate Bi^{3+} typical emission. The stacked VRBE diagram in Figure 1a and column 7 of Table 2 further show that the VRBE at the conduction band bottom (E_C) slightly changes when replacing Lu for Y in $NaREGeO_4$. It means that one may tailor the glow peak temperature due to electron liberation from Eu^{2+} or Bi^{2+} and recombination with holes at Bi^{4+} through engineering the VRBE at the CB bottom.

The results for $NaLu_{1-x}Y_xGeO_4$ solid solutions in Figures 7a and 8a show this tailoring. With increasing x, the TL glow peak related to electron release from Bi^{2+} shifts about 69 K from 226 to ∼295 K in $NaLu_{1-x}Y_xGeO_4$:0.01Bi^{3+}, and the TL peak related to electron release from Eu^{2+} shifts about 41 K from 356 to 397 K in $NaLu_{1-x}Y_xGeO_4$:0.01Bi^{3+},0.001Eu^{3+}. For the trap depth difference, a value of ∼0.1 or ∼0.16 eV is respectively derived from the Eu^{2+} or Bi^{2+} TL peaks in Table 1. This means that the CB bottom moves up about 0.1−0.16 eV when Lu is replaced by Y in $NaLu_{1-x}Y_xGeO_4$. This is consistent with the 0.07 eV difference in the VRBE scheme in Figure 1a when considering the error margins in the VRBE

https://dx.doi.org/10.1021/acs.chemmater.9b04341
Chem. Mater. 2020, 32, 1192−1209

scheme based on broad CT-band transitions and the errors in the derived trap depth by TL measurement.[19] The above TL results also support our assumption that the VRBE in the Bi^{2+} ground state is near −3.5 ± 0.5 eV[45] for $NaREGeO_4$ (RE = Y, Lu). More specifically, with the Bi^{3+} electron trap depth in column 6 of Table 1 and E_C in column 7 of Table 2, the VRBE in the Bi^{2+} $^2P_{1/2}$ ground state is determined to be near −3.2 and −3.3 eV for $NaLuGeO_4$ and $NaYGeO_4$, respectively.

Bi^{3+} afterglow appears when the TL glow peak for electron release from Bi^{2+} nicely shifts to near 295 K with increasing x in $NaLu_{1-x}Y_xGeO_4$ in Figure 7a. The Bi^{2+} TL peak and afterglow intensity are found to be enhanced via optimizing synthesis temperature in Figure 7b−d and synthesis duration time in Figure 7e−g. Note that the Bi^{2+} TL peak maximum changes between 269 and 300 K with increasing temperature from 1100 to 1300 °C, implying that the VRBE at the conduction band and/or the Bi^{2+} ground state slightly (∼0.1 eV) depends on the synthesis temperature. Figure 7e shows that the Bi^{2+} TL peak intensity near 358 K increases about 7 times when the synthesis duration time increases from 3 to 24 h at 1200 °C. Small crystals of about 1−5 μm tend to form aggregates at 3 h synthesis duration in Figure S13a (SI). With increasing synthesis duration time to 24 h in Figure S13e,f (SI), aggregates of about 5−20 μm appear, which may either increase the number of Bi^{3+} electron traps or promote the capture of free electrons during β-ray charging. Figure 7h shows that the Bi^{2+} TL peak intensity was found to further increase about 2.5 times when the doped Bi^{3+} concentration decreases from 1% to 0.1% or when 25% Na^+ is replaced by Li^+ to form solid solution $Na_{0.75}Li_{0.25}YGeO_4$:0.01Bi^{3+}. The crystal synthesis optimization and composition modulation showed that one may engineer afterglow phosphor performance, and here the optimized TL intensity of both $NaYGeO_4$:0.001Bi^{3+} and $Na_{0.75}Li_{0.25}YGeO_4$:0.01Bi^{3+} is about 4 and 3 times higher than that of the commercial $SrAl_2O_4$:Eu,Dy and BaFBr(I):Eu phosphors after β-irradiation in Figure 7h.

With increasing x in $NaLu_{1-x}Y_xGeO_4$:0.01Bi^{3+},0.001Eu^{3+}, the Eu^{2+} glow peak, like that of Bi^{2+} above, shifts toward higher temperature, which leads to the formation of a Bi^{3+} storage phosphor in Figure 8c. This is consistent with the decrease of the initial Bi^{3+} afterglow intensity in Figure 8d and the weaker TL fading in Figure 8e. Figure S12a (SI) shows the TL glow peaks for $NaYGeO_4$:0.01Bi^{3+},$x$$Eu^{3+}$. The TL peak intensity first increases and then decrease gradually when x > 0.1%. Appropriate content of 0.1% Eu^{3+} can produce enough Eu^{3+} electron traps, but more Eu^{3+} also leads to an enhanced energy transfer from Bi^{3+} → Eu^{3+}, leading to increased Eu^{3+} emission in Figure 6b−d, to which the used photomultiplier tube is not sensitive. This slow Eu^{3+} 4f−4f transition is not suitable for an optically stimulated storage phosphor. Note that Bi^{3+} emission near 350−500 nm in Figure S3b (SI) with 0.33 μs decay time in Figure S24 (SI) appears to match well with the traditional photomultiplier tube.

The band at 230 nm in the RT thermoluminescence excitation (TLE) spectra of $NaLu_{1-x}Y_xGeO_4$:0.01Bi^{3+} or 0.01Bi^{3+},0.001Eu^{3+} in Figure 9c3−c11 coincides with the Bi^{3+} D-band in Figure 9c1 but also the VB → Eu^{3+} CT-band in Figure 9c2. During D-band excitation like in Figure 1b, electrons are excited from the Bi^{3+} $^1S_0$ ground state to the conduction band and are subsequently captured at intentional defects such as Bi^{3+} and Eu^{3+} or other host intrinsic defects, like those responsible for the TL peaks near 492, 562, and 666 K in Figure 9a. For VB → Eu^{3+} CT-band excitation, electrons are excited from the valence band to Eu^{2+} $4f^7$ ground state and holes are produced in the valence band that can subsequently be trapped by intrinsic host hole traps or a Bi^{3+} hole trap center to form Bi^{4+}.[19,62] For both alternatives, Eu^{2+} and Bi^{4+} are created. In the former one, additional intrinsic electron traps are charged, and in the latter one, additional intrinsic hole traps are charged. Figure 7a shows that the electrons captured at Bi^{2+} in $NaYGeO_4$ have already gone because of recombination with holes at Bi^{4+} near 300 K. Therefore, the Eu^{2+} TL glow peak near 422 K and other TL peaks near 484, 560, and 662 K in $NaYGeO_4$:0.01Bi^{3+},0.001Eu^{3+} in Figure 9b cannot be attributed to hole release from Bi^{4+} or other host intrinsic hole traps to recombine with electrons at Bi^{2+}, giving Bi^{3+} emission. Note that these TL peaks at ∼484, 560, and 662 K can also be observed in $NaYGeO_4$:0.01Bi^{3+} in Figure 9a. The charging route in $NaYGeO_4$:0.01Bi^{3+},0.001Eu^{3+} is then likely realized via the Bi^{3+} D-band instead of the VB → Eu^{3+} CT-band. During TL readout in Figure 9a,b, the electrons first liberate from Bi^{2+}, Eu^{2+}, or host intrinsic defects to recombine with holes at Bi^{4+} to produce Bi^{3+} A-band emission and Eu^{3+} 4f−4f emission via energy transfer from Bi^{3+}. On the basis of the VRBE scheme for $NaYGeO_4$ in Figure 1b, the Bi^{3+} excited $^3P_1$ state is ∼1.2 eV below the CB bottom. This gap is too large to enable effective thermal ionization of an electron from the $^3P_1$ excited state to the CB bottom at RT. This explains why Bi^{3+} has an intense A-band excitation but A-band excitation cannot charge the phosphor in Figure 9.

4.3. Anti-Counterfeiting Application and Information Storage Using Bi^{3+} Afterglow and Storage Phosphors.

Figure 14 shows the photoelectric absorption coefficient for $NaLu_{1-x}Y_xSiO_4$ (x = 0, 0.5, 0.75, and 1). At 20 keV, $NaLu_{1-x}Y_xSiO_4$ has 10% more absorption than BaFBr. This implies that a $NaLu_{1-x}Y_xSiO_4$ phosphor receives the same dose as BaFBr as a lower X-ray exposure to the patient. At E = 150 keV, the photoelectric absorption ratio of $NaLu_{1-x}Y_xSiO_4$ to BaFBr increases from 0.27 for x = 1 to 1.64 for x = 0 because more lutetium ions lead to more photoelectric absorption of X-rays.

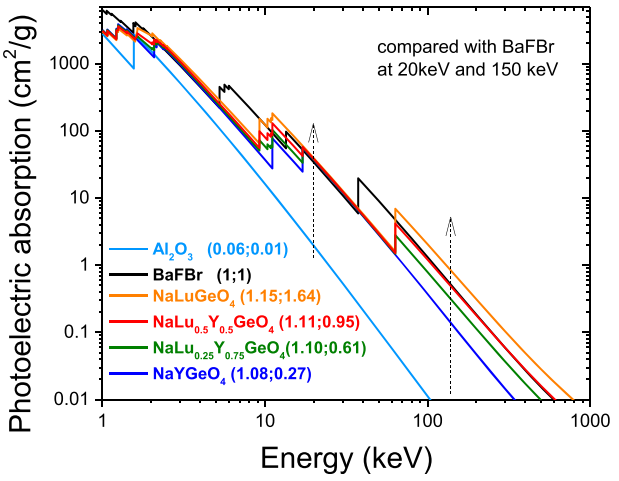

Figure 14. Photoelectric absorption coefficient for $NaLu_{1-x}Y_xSiO_4$, Al_2O_3, and BaFBr. The arrows demonstrate the characteristic energies for mammography at 20 keV and bone radiography at 150 keV.

https://dx.doi.org/10.1021/acs.chemmater.9b04341
Chem. Mater. 2020, 32, 1192−1209

We concluded that only the Bi^{3+} D-band near 230 nm can charge $NaYGeO_4$:0.01Bi^{3+} and $NaYGeO_4$:0.01Bi^{3+},0.001Eu^{3+} phosphors. It means that it is not necessary to keep the storage phosphor $NaYGeO_4$:0.01Bi^{3+},0.001Eu^{3+} in the dark during X-ray charging. To develop a Bi^{3+} afterglow phosphor that can be charged by sunlight, one has to use a compound with a relatively low energy Bi^{3+} D-band. $CaMoO_4$[63] with 3.83 eV and $ScVO_4$[64] with 3.49 eV are such compounds. One may also try compounds like $Y_3Ga_5O_{12}$,[44] in which the Bi^{3+} $^3P_1$ excited state is close to the CB bottom.

The red emission in Figure 12b3 is attributed to a reabsorption process of $NaYGeO_4$:0.01Bi^{3+} afterglow by $CsPbBr_3$ and CdSe QDs. One supporting evidence is the spectral overlap between the Bi^{3+} A-band emission near 350−500 nm in Figure 12a3 and the broad 200−475 nm excitation band for $CsPbBr_3$ and CdSe QDs[65,66] in Figure S23 (SI). Another one is that a large decrease of lifetime of the Bi^{3+} $^3P_1 \rightarrow {}^1S_0$ is not observed in films 1 and 2 as compared with $NaYGeO_4$:0.01Bi^{3+} in Figure S24 (SI). Note that the emission of $CsPbBr_3$ QDs near 520 nm overlaps with the excitation spectrum of CdSe QDs in Figure S23 (SI). This means that the green emission of $CsPbBr_3$ QDs can partly be reabsorbed by CdSe QDs. Decreasing the ratio of CdSe to $CsPbBr_3$ QDs can generate less red emission from CdSe QDs, which leads to the color change from red in film 1 to cyan in film 2.

5. CONCLUSIONS

A design principle to discover, develop, and optimize new afterglow and storage phosphors for energy storage was demonstrated by combining vacuum-referred binding energy (VRBE) diagrams, band structure engineering, and crystal synthesis optimization. On the basis of previous research for the $LiLuSiO_4$ compound, the $ARE(Si,Ge)O_4$ (A = Li, Na; RE = Y, Lu) crystal system was selected after screening the Pearson's crystal data. Low-temperature spectroscopy for lanthanides- and bismuth-doped $ARE(Si,Ge)O_4$ was first studied. This was used to establish the stacked VRBE schemes for $ARE(Si,Ge)O_4$ with the VRBE in lanthanide and bismuth energy levels, which guide us in the interpretation of spectra and TL results and eventually to design charge-carrier-trapping processes. As a demonstration, Bi^{3+} afterglow and storage phosphors were explored in $NaLu_{1-x}Y_xGeO_4$. By combining Bi^{3+} with Bi^{3+} itself or Eu^{3+}, Bi^{3+} emerges to act as deep hole-capturing center, while Bi^{3+} and Eu^{3+} act as less-deep electron traps. Trap depth tunable Bi^{3+} afterglow and storage phosphors respectively appear in $NaLu_{1-x}Y_xGeO_4$:0.01Bi^{3+} and $NaLu_{1-x}Y_xGeO_4$:0.01Bi^{3+},0.001Eu^{3+} via changing x, resulting in conduction band engineering. More than 28 h of Bi^{3+} afterglow was measurable in $NaYGeO_4$:0.01Bi^{3+} due to electron release from Bi^{2+} and recombination with a hole at Bi^{4+}. The charge carrier storage capacity in $NaYGeO_4$:0.01Bi^{3+} was found to increase ∼7 times through optimizing synthesis conditions at 1200 °C during 24 h. The thermoluminescence (TL) intensity of the optimized $NaYGeO_4$:0.001Bi^{3+} and $NaYGeO_4$:0.01Bi^{3+},0.001Eu^{3+} is ∼3, and ∼7 times higher than the TL of the commercial X-ray storage phosphor BaFBr(I):Eu, respectively. Proof-of-concept color tuning for anti-counterfeiting application was demonstrated by mixing the discovered and optimized $NaYGeO_4$:0.01Bi^{3+} afterglow phosphor with perovskite $CsPbBr_3$ and CdSe quantum dots. Information storage application was demonstrated by UV-light- or X-ray-charged $NaYGeO_4$:0.01Bi^{3+},0.001Eu^{3+} phosphor dispersed in a silicone gel imaging film. This work not only reports excellent afterglow and storage phosphors but more importantly provides a general design principle through combining VRBE scheme guided band structure engineering and crystal synthesis optimization. Therefore, it can enable discovery of new afterglow and storage phosphors for energy storage in a designed way instead of by a traditional trial-and-error approach.

■ ASSOCIATED CONTENT

Supporting Information

The Supporting Information is available free of charge at https://pubs.acs.org/doi/10.1021/acs.chemmater.9b04341.

Additional VRBE diagrams, XRD data, photoluminescence excitation and emission spectra, thermoluminescence emission spectra, thermoluminescence glow curves, thermoluminescence excitation spectra, isothermal afterglow decay curve, SEM images, fluorescence decay curves, and photographs (Figures S1−S26, Table S1) (PDF)

Movie showing antifake application on paper in the dark using Bi^{3+} afterglow from $NaYGeO_4$:0.01Bi^{3+} as backlight (MOV)

Movie showing anti-counterfeiting application with text display by combining Bi^{3+} afterglow from $NaYGeO_4$:0.01Bi^{3+} with $CsPbBr_3$ and CdSe QDs (MOV)

Movie showing text storage and display application with $NaYGeO_4$:1%Bi^{3+},0.1%Eu^{3+} heated at ∼380 K in the dark (MOV)

Movie showing bone-imaging storage and display application with X-ray-charged $NaYGeO_4$:1%Bi^{3+},0.1%Eu^{3+} film heated at ∼380 K with different duration in the dark (MOV)

■ AUTHOR INFORMATION

Corresponding Author

Tianshuai Lyu − *Delft University of Technology, Delft, The Netherlands;* orcid.org/0000-0002-5714-6161; Email: T.lyu-1@tudelft.nl

Other Author

Pieter Dorenbos − *Delft University of Technology, Delft, The Netherlands*

Complete contact information is available at: https://pubs.acs.org/10.1021/acs.chemmater.9b04341

Notes

The authors declare no competing financial interest.

■ ACKNOWLEDGMENTS

T. Lyu. acknowledges the financial support from the China Scholarship Council for his Ph.D. research (Tianshuai Lyu: 201608320151). We thank Drs. Adrie J. J. Bos and Jaco Geuchies for providing the Al_2O_3:C single crystal, $CsPbBr_3$ and CdSe quantum dots, and Dr. Giacomo B. F. Bosco for SEM measurement at the Delft University of Technology.

■ REFERENCES

(1) Shi, H.; An, Z. Ultraviolet afterglow. *Nat. Photonics* **2019**, *13* (2), 74−75.

(2) Gao, Y.; Li, R.; Zheng, W.; Shang, X.; Wei, J.; Zhang, M.; Xu, J.; You, W.; Chen, Z.; Chen, X. Broadband NIR photostimulated

luminescence nanoprobes based on CaS:Eu^{2+},Sm^{3+} nanocrystals. *Chemical Science* **2019**, *10* (21), 5452−5460.
(3) Fan, W.; Tang, W.; Lau, J.; Shen, Z.; Xie, J.; Shi, J.; Chen, X. Breaking the Depth Dependence by Nanotechnology-Enhanced X-Ray-Excited Deep Cancer Theranostics. *Adv. Mater.* **2019**, *31* (12), 1806381.
(4) Yang, Y.-M.; Li, Z.-Y.; Zhang, J.-Y.; Lu, Y.; Guo, S.-Q.; Zhao, Q.; Wang, X.; Yong, Z.-J.; Li, H.; Ma, J.-P.; Kuroiwa, Y.; Moriyoshi, C.; Hu, L.-L.; Zhang, L.-Y.; Zheng, L.-R.; Sun, H.-T. X-ray-activated long persistent phosphors featuring strong UVC afterglow emissions. *Light: Sci. Appl.* **2018**, *7* (1), 88.
(5) Dobrowolska, A.; Bos, A. J. J.; Dorenbos, P. High Charge Carrier Storage Capacity in Lithium Lutetium Silicate Doped with Cerium and Thulium. *Phys. Status Solidi RRL* **2019**, *13* (3), 1800502.
(6) Seggern, H. v. Photostimulable x-ray storage phosphors: a review of present understanding. *Braz. J. Phys.* **1999**, *29*, 254−268.
(7) Cameron, J. R.; Zimmerman, D.; Kenney, G.; Buch, R.; Bland, R.; Grant, R. Thermoluminescent Radiation Dosimetry Utilizing LiF. *Health Phys.* **1964**, *10* (1), 25−29.
(8) Cameron, J. R.; Daniels, F.; Johnson, N.; Kenney, G. Radiation Dosimeter Utilizing the Thermoluminescence of Lithium Fluoride. *Science* **1961**, *134* (3475), 333−334.
(9) McKeever, S. W. S.; Moscovitch, M.; Townsend, P. D. *Thermoluminescence Dosimetry Materials: Properties and Uses*; Nuclear Technology Publishing, 1995.
(10) Bedard, A.; Davis, T. D.; Angelopoulos, C. Storage phosphor plates: how durable are they as a digital dental radiographic system. *J. Contemp Dent Pract* **2004**, *5* (2), 57−69.
(11) Leblans, P.; Vandenbroucke, D.; Willems, P. Storage Phosphors for Medical Imaging. *Materials* **2011**, *4* (6), 1034.
(12) Thoms, M.; von Seggern, H.; Winnacker, A. Spatial correlation and photostimulability of defect centers in the x-ray-storage phosphor BaFBr:Eu^{2+}. *Phys. Rev. B: Condens. Matter Mater. Phys.* **1991**, *44* (17), 9240−9247.
(13) Li, Y.; Gecevicius, M.; Qiu, J. Long persistent phosphors-from fundamentals to applications. *Chem. Soc. Rev.* **2016**, *45* (8), 2090−2136.
(14) Lyu, T.; Dorenbos, P. Designing thermally stimulated 1.06 μm Nd^{3+} emission for the second bio-imaging window demonstrated by energy transfer from Bi^{3+} in La-, Gd-, Y-, and $LuPO_4$. *Chem. Eng. J.* **2019**, *372*, 978−991.
(15) Ren, W.; Lin, G.; Clarke, C.; Zhou, J.; Jin, D. Optical Nanomaterials and Enabling Technologies for High-Security-Level Anticounterfeiting. *Adv. Mater.* **2019**, *0* (0), 1901430.
(16) Liu, Z.; Zhao, L.; Chen, W.; Fan, X.; Yang, X.; Tian, S.; Yu, X.; Qiu, J.; Xu, X. Multiple anti-counterfeiting realized in $NaBaScSi_2O_7$ with a single activator of Eu^{2+}. *J. Mater. Chem. C* **2018**, *6* (41), 11137−11143.
(17) Sun, Z.; Yang, J.; Huai, L.; Wang, W.; Ma, Z.; Sang, J.; Zhang, J.; Li, H.; Ci, Z.; Wang, Y. Spy Must Be Spotted: A Multistimuli-Responsive Luminescent Material for Dynamic Multimodal Anti-counterfeiting and Encryption. *ACS Appl. Mater. Interfaces* **2018**, *10* (25), 21451−21457.
(18) Zhang, J.-C.; Pan, C.; Zhu, Y.-F.; Zhao, L.-Z.; He, H.-W.; Liu, X.; Qiu, J. Achieving Thermo-Mechano-Opto-Responsive Bitemporal Colorful Luminescence via Multiplexing of Dual Lanthanides in Piezoelectric Particles and its Multidimensional Anticounterfeiting. *Adv. Mater.* **2018**, *30* (49), 1804644.
(19) Lyu, T.; Dorenbos, P. Charge carrier trapping processes in lanthanide doped $LaPO_4$, $GdPO_4$, YPO_4, and $LuPO_4$. *J. Mater. Chem. C* **2018**, *6* (2), 369−379.
(20) Smet, P. F.; Botterman, J.; Van den Eeckhout, K.; Korthout, K.; Poelman, D. Persistent luminescence in nitride and oxynitride phosphors: A review. *Opt. Mater.* **2014**, *36* (11), 1913−1919.
(21) Lakshmanan, A. R. Radiation induced defects and photo-stimulated luminescence process in BaFBr: Eu^{2+}. *physica status solidi (a)* **1996**, *153* (1), 3−27.
(22) Schweizer, S. Physics and Current Understanding of X-Ray Storage Phosphors. *physica status solidi (a)* **2001**, *187* (2), 335−393.
(23) Takahashi, K.; Kohda, K.; Miyahara, J.; Kanemitsu, Y.; Amitani, K.; Shionoya, S. Mechanism of photostimulated luminescence in BaFX:Eu^{2+} (X = Cl,Br) phosphors. *J. Lumin.* **1984**, *31*−*32*, 266−268.
(24) Rüter, H. H.; Seggern, H. v.; Reininger, R.; Saile, V. Creation of photostimulable centers in BaFBr:Eu^{2+} single crystals by vacuum ultraviolet radiation. *Phys. Rev. Lett.* **1990**, *65* (19), 2438−2441.
(25) von Seggern, H.; Voigt, T.; Knüpfer, W.; Lange, G. Physical model of photostimulated luminescence of x-ray irradiated BaFBr:Eu^{2+}. *J. Appl. Phys.* **1988**, *64* (3), 1405−1412.
(26) Schweizer, S.; Hobbs, L. W.; Secu, M.; Spaeth, J.-M.; Edgar, A.; Williams, G. V. M. Photostimulated luminescence in Eu-doped fluorochlorozirconate glass ceramics. *Appl. Phys. Lett.* **2003**, *83* (3), 449−451.
(27) Riesen, H.; Kaczmarek, W. A. Efficient X-ray Generation of Sm^{2+} in Nanocrystalline BaFCl/Sm^{3+}: a Photoluminescent X-ray Storage Phosphor. *Inorg. Chem.* **2007**, *46* (18), 7235−7237.
(28) Yanagida, T.; Okada, G.; Kawaguchi, N. Ionizing-radiation-induced storage-luminescence for dosimetric applications. *J. Lumin.* **2019**, *207*, 14−21.
(29) Xu, J.; Tanabe, S. Persistent luminescence instead of phosphorescence: History, mechanism, and perspective. *J. Lumin.* **2019**, *205*, 581−620.
(30) Van den Eeckhout, K.; Smet, P. F.; Poelman, D. Persistent luminescence in Eu^{2+}-doped compounds: a review. *Materials* **2010**, *3*, 2536.
(31) Pan, Z.; Lu, Y.-Y.; Liu, F. Sunlight-activated long-persistent luminescence in the near-infrared from Cr^{3+}-doped zinc gallogermanates. *Nat. Mater.* **2012**, *11* (1), 58−63.
(32) Yang, M.-M.; Iqbal, A. N.; Peters, J. J. P.; Sanchez, A. M.; Alexe, M. Strain-gradient mediated local conduction in strained bismuth ferrite films. *Nat. Commun.* **2019**, *10* (1), 2791.
(33) Leng, M.; Yang, Y.; Zeng, K.; Chen, Z.; Tan, Z.; Li, S.; Li, J.; Xu, B.; Li, D.; Hautzinger, M. P.; Fu, Y.; Zhai, T.; Xu, L.; Niu, G.; Jin, S.; Tang, J. All-Inorganic Bismuth-Based Perovskite Quantum Dots with Bright Blue Photoluminescence and Excellent Stability. *Adv. Funct. Mater.* **2018**, *28* (1), 1704446.
(34) Noguchi, R.; Takahashi, T.; Kuroda, K.; Ochi, M.; Shirasawa, T.; Sakano, M.; Bareille, C.; Nakayama, M.; Watson, M. D.; Yaji, K.; Harasawa, A.; Iwasawa, H.; Dudin, P.; Kim, T. K.; Hoesch, M.; Kandyba, V.; Giampietri, A.; Barinov, A.; Shin, S.; Arita, R.; Sasagawa, T.; Kondo, T. A weak topological insulator state in quasi-one-dimensional bismuth iodide. *Nature* **2019**, *566* (7745), 518−522.
(35) Han, J.; Pan, F.; Molokeev, M. S.; Dai, J.; Peng, M.; Zhou, W.; Wang, J. Redefinition of Crystal Structure and Bi^{3+} Yellow Luminescence with Strong Near-Ultraviolet Excitation in La_3BWO_9:Bi^{3+} Phosphor for White Light-Emitting Diodes. *ACS Appl. Mater. Interfaces* **2018**, *10* (16), 13660−13668.
(36) Sun, H.-T.; Zhou, J.; Qiu, J. Recent advances in bismuth activated photonic materials. *Prog. Mater. Sci.* **2014**, *64*, 1−72.
(37) Swart, H. C.; Kroon, R. E. Ultraviolet and visible luminescence from bismuth doped materials. *Optical Materials: X* **2019**, *2*, 100025.
(38) Lyu, T.; Dorenbos, P. Bi^{3+} acting both as an electron and as a hole trap in La-, Y-, and $LuPO_4$. *J. Mater. Chem. C* **2018**, *6* (23), 6240−6249.
(39) Wang, X.; Boutinaud, P.; Li, L.; Cao, J.; Xiong, P.; Li, X.; Luo, H.; Peng, M. Novel persistent and tribo-luminescence from bismuth ion pairs doped strontium gallate. *J. Mater. Chem. C* **2018**, *6* (38), 10367−10375.
(40) Sun, W.; Pang, R.; Li, H.; Li, D.; Jiang, L.; Zhang, S.; Fu, J.; Li, C. Investigation of a novel color tunable long afterglow phosphor $KGaGeO_4$:Bi^{3+}: luminescence properties and mechanism. *J. Mater. Chem. C* **2017**, *5* (6), 1346−1355.
(41) Wang, W.; Sun, Z.; He, X.; Wei, Y.; Zou, Z.; Zhang, J.; Wang, Z.; Zhang, Z.; Wang, Y. How to design ultraviolet emitting persistent materials for potential multifunctional applications: a living example of a $NaLuGeO_4$:Bi^{3+},Eu^{3+} phosphor. *J. Mater. Chem. C* **2017**, *5* (17), 4310−4318.

(42) Dorenbos, P. A Review on How Lanthanide Impurity Levels Change with Chemistry and Structure of Inorganic Compounds. *ECS J. Solid State Sci. Technol.* **2013**, *2* (2), R3001−R3011.
(43) Dorenbos, P. Charge transfer bands in optical materials and related defect level location. *Opt. Mater.* **2017**, *69*, 8−22.
(44) Awater, R. H. P.; Dorenbos, P. The Bi^{3+} 6s and 6p electron binding energies in relation to the chemical environment of inorganic compounds. *J. Lumin.* **2017**, *184*, 221−231.
(45) Awater, R. H. P.; Dorenbos, P. Towards a general concentration quenching model of Bi^{3+} luminescence. *J. Lumin.* **2017**, *188*, 487−489.
(46) Dorenbos, P. Modeling the chemical shift of lanthanide 4f electron binding energies. *Phys. Rev. B: Condens. Matter Mater. Phys.* **2012**, *85* (16), 165107.
(47) Bos, A. J. J.; van Duijvenvoorde, R. M.; van der Kolk, E.; Drozdowski, W.; Dorenbos, P. Thermoluminescence excitation spectroscopy: A versatile technique to study persistent luminescence phosphors. *J. Lumin.* **2011**, *131* (7), 1465−1471.
(48) Sidorenko, A. V.; Dorenbos, P.; Bos, A. J. J.; van Eijk, C. W. E.; Rodnyi, P. A. Lanthanide level location and charge carrier trapping in $LiLnSiO_4$:Ce^{3+}, Sm^{3+}, Ln = Y or Lu. *J. Phys.: Condens. Matter* **2006**, *18* (19), 4503−4514.
(49) Blasse, G.; Bril, A. Structure and Eu^{3+}-fluorescence of lithium and sodium lanthanide silicates and germanates. *J. Inorg. Nucl. Chem.* **1967**, *29* (9), 2231−2241.
(50) Oomen, E. W. J. L.; Smit, W. M. A.; Blasse, G. Jahn-Teller effect in the emission and excitation spectra of the Sb^{3+} ion in LPO_4 (L = Sc,Lu,Y). *Phys. Rev. B: Condens. Matter Mater. Phys.* **1988**, *37* (1), 18−26.
(51) Fukuda, A. Jahn-Teller Effect on the Structure of the Emission Produced by Excitation in the A Band of KI: Tl-Type Phosphors. Two Kinds of Minima on the $^3T_{1u}$ Adiabatic Potential-Energy Surface. *Phys. Rev. B* **1970**, *1* (10), 4161−4178.
(52) Hoogenstraaten, W. Electron traps in zinc−sulphide phosphors. *Philips Res. Rep* **1958**, *13*, 515−693.
(53) Chen, R.; Winer, S. A. A. Effects of Various Heating Rates on Glow Curves. *J. Appl. Phys.* **1970**, *41* (13), 5227−5232.
(54) Azorín, J. Determination of thermoluminescence parameters from glow curves—I. A review. *International Journal of Radiation Applications and Instrumentation. Part D. Nuclear Tracks and Radiation Measurements* **1986**, *11* (3), 159−166.
(55) Liu, X.; Li, L.; Noh, H. M.; Moon, B. K.; Choi, B. C.; Jeong, J. H. Chemical bond properties and charge transfer bands of O^{2-}−Eu^{3+}, O^{2-}−Mo^{6+} and O^{2-}−W^{6+} in Eu^{3+}-doped garnet hosts $Ln_3M_5O_{12}$ and ABO_4 molybdate and tungstate phosphors. *Dalton Transactions* **2014**, *43* (23), 8814−8825.
(56) Luo, H.; Ning, L.; Dong, Y.; Bos, A. J. J.; Dorenbos, P. Electronic Structure and Site Occupancy of Lanthanide-Doped $(Sr, Ca)_3(Y, Lu)_2Ge_3O_{12}$ Garnets: A Spectroscopic and First-Principles Study. *J. Phys. Chem. C* **2016**, *120* (50), 28743−28752.
(57) Dobrowolska, A.; Bos, A. J. J.; Dorenbos, P. Synthesis optimization and charge carrier transfer mechanism in $LiLuSiO_4$:Ce, Tm storage phosphor. *Radiat. Meas.* **2019**, *127*, 106147.
(58) Dorenbos, P. The Pr^{3+} and Tb^{3+} ground state locations in compounds obtained from thermoluminescence and intervalence charge transfer studies. *Opt. Mater.* **2019**, *91*, 333−337.
(59) Boutinaud, P.; Bettinelli, M.; Diaz, F. Intervalence charge transfer in Pr^{3+}- and Tb^{3+}-doped double tungstate crystals $KRE(WO_4)_2$ (RE = Y, Gd, Yb, Lu). *Opt. Mater.* **2010**, *32* (12), 1659−1663.
(60) Liu, C.; Pan, F.; Peng, Q.; Zhou, W.; Shi, R.; Zhou, L.; Zhang, J.; Chen, J.; Liang, H. Excitation Wavelength Dependent Luminescence of $LuNbO_4$:Pr^{3+}—Influences of Intervalence Charge Transfer and Host Sensitization. *J. Phys. Chem. C* **2016**, *120* (45), 26044−26053.
(61) Wang, L.; Sun, Q.; Liu, Q.; Shi, J. Investigation and application of quantitative relationship between sp energy levels of Bi^{3+} ion and host lattice. *J. Solid State Chem.* **2012**, *191*, 142−146.
(62) Luo, H.; Bos, A. J. J.; Dorenbos, P. Charge Carrier Trapping Processes in RE_2O_2S (RE = La, Gd, Y, and Lu). *J. Phys. Chem. C* **2017**, *121* (16), 8760−8769.
(63) Boutinaud, P.; Cavalli, E. Predicting metal-to-metal charge transfer in closed-shell transition metal oxides doped with Bi^{3+} or Pb^{2+}. *Chem. Phys. Lett.* **2011**, *503* (4), 239−243.
(64) Kang, F.; Yang, X.; Peng, M.; Wondraczek, L.; Ma, Z.; Zhang, Q.; Qiu, J. Red Photoluminescence from Bi^{3+} and the Influence of the Oxygen-Vacancy Perturbation in $ScVO_4$: A Combined Experimental and Theoretical Study. *J. Phys. Chem. C* **2014**, *118* (14), 7515−7522.
(65) Wei, Y.; Cheng, Z.; Lin, J. An overview on enhancing the stability of lead halide perovskite quantum dots and their applications in phosphor-converted LEDs. *Chem. Soc. Rev.* **2019**, *48* (1), 310−350.
(66) Mongin, C.; Moroz, P.; Zamkov, M.; Castellano, F. N. Thermally activated delayed photoluminescence from pyrenyl-functionalized CdSe quantum dots. *Nat. Chem.* **2018**, *10*, 225.

https://dx.doi.org/10.1021/acs.chemmater.9b04341
Chem. Mater. 2020, 32, 1192−1209